HHS Public Access

Author manuscript

Dev Cell. Author manuscript; available in PMC 2022 January 11.

Published in final edited form as:

Dev Cell. 2021 January 11; 56(1): 95–110.e10. doi:10.1016/j.devcel.2020.10.014.

Stromal upregulation of SOX2 promotes tumorigenesis through the generation of a SFRP1/2-expressing cancer-associated fibroblast population

Hiroaki Kasashima[1,2], **Angeles Duran**[1,2], **Anxo Martinez-Ordoñez**[2], **Yuki Nakanishi**[1], **Hiroto Kinoshita**[1,2], **Juan F. Linares**[2], **Miguel Reina-Campos**[1], **Yotaro Kudo**[1], **Antoine L'Hermitte**[1], **Masakazu Yashiro**[3], **Masaichi Ohira**[3], **Fei Bao**[4], **Daniele V.F. Tauriello**[5,6], **Eduard Batlle**[7,8], **Maria T. Diaz-Meco**[1,2,*], **Jorge Moscat**[1,2,9,*]

[1]Sanford Burnham Prebys Medical Discovery Institute, 10901 N. Torrey Pines Road, La Jolla, CA 92037, USA [2]Department of Pathology and Laboratory Medicine, Weill Cornell Medicine, 1300 York Avenue, New York, NY 10065, USA [3]Department of Gastroenterological Surgery, Osaka City University Graduate School of Medicine, Osaka city, Japan [4]Department of Pathology, Scripps Clinic, La Jolla, CA 92037, USA [5]Institute for Research in Biomedicine (IRB Barcelona), The Barcelona Institute of Science and Technology, Baldiri i Reixac 10, 08028 Barcelona, Spain [6]Department of Cell Biology, Radboud Institute for Molecular Life Sciences, Radboud University Medical Center, Nijmegen, The Netherlands [7]ICREA, Passeig Lluís Companys 23, 08010 Barcelona, Spain. [8]Centro de Investigación Biomédica en Red de Cáncer (CIBERONC), Barcelona, Spain [9]Lead Contact

SUMMARY

Cancer-associated fibroblasts (CAFs) promote tumor malignancy, but the precise transcriptional mechanisms regulating the acquisition of the CAF phenotype are not well understood. We show that the upregulation of SOX2 is central to this process, which is repressed by protein kinase Cζ (PKCζ). PKCζ deficiency activates the reprogramming of colonic fibroblasts to generate a predominant SOX2-dependent CAF population expressing the WNT regulator *Sfrp2* as its top biomarker. SOX2 directly binds the *Sfrp1/2* promoters, and the inactivation of *Sox2 or Sfrp1/2* in CAFs impaired the induction of migration and invasion of colon cancer cells, as well as their tumorigenicity in vivo. Importantly, recurrence-free and overall survival of colorectal cancer (CRC) patients negatively correlates with stromal PKCζ levels. Also, SOX2 expression in the stroma is associated with CRC T invasion and worse prognosis of recurrence-free survival.

*Correspondences: jom4010@med.cornell.edu (J.M.); mtd4001@med.cornell.edu (M.T.D-M).

AUTHOR CONTRIBUTIONS

Conceptualization, M.T.D.-M., J.M., and H.K.; Methodology, D.V.F.T.; Investigation, H.K., A.D., A.M.-O., Y.N., H.K., J.F.L., M.R.-C., Y.K., A.L'H.; Resources, D.V.F.T., E.B., M.Y., M.O., F.B.; Writing – Original Draft, M.T.D.-M., J.M., and H.K.; Writing – Review & Editing, all authors; Supervision, M.T.D.-M., and J.M.; Funding Acquisition, M.T.D.-M., and J.M.

DECLARATION OF INTERESTS

The authors declare no competing interests.

Therefore, the PKCζ-SOX2 axis emerges as a critical step in the control of CAF pro-tumorigenic potential.

Graphical Abstract

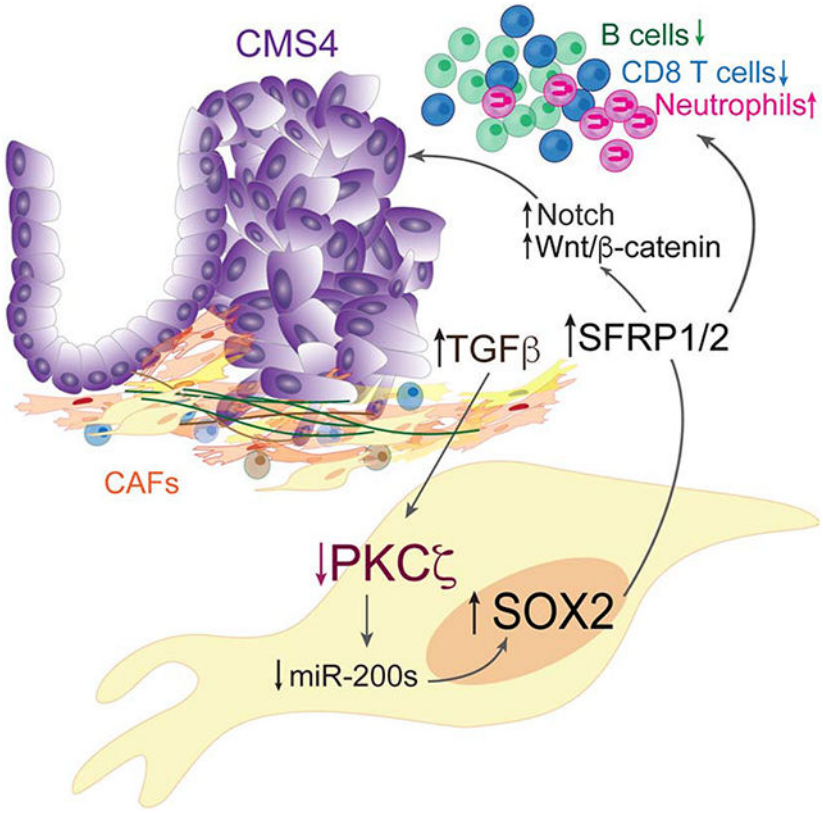

eTOC

Kasashima et al. describe a molecular mechanism whereby the loss of PKCz in the stroma upregulates SOX2 to activate the reprogramming of colonic fibroblasts generating a SFRP1/2-expressing CAF population. This population supports epithelial tumor progression, revealing vulnerabilities in mesenchymal CMS4 colorectal cancer.

INTRODUCTION

CAFs impact a large variety of functions in the tumor epithelium by secreting growth factors and inflammatory mediators, reprogramming their metabolism to provide nutrients for epithelial cancer cell proliferation, promoting angiogenesis that favors the tumor access to nutrients and oxygen, and remodeling the extracellular matrix (Hanahan and Weinberg, 2011; Kalluri, 2016; Linares et al., 2017; Quail and Joyce, 2013; Sousa et al., 2016). Besides, CAFs contribute to the creation of immunosuppressed microenvironments that impair immunosurveillance and favor cancer initiation and progression (De Jaeghere et al., 2019; Guinney et al., 2015; Nakanishi et al., 2019). The extensive heterogeneity of secreted molecules, and the wide variety of extracellular interactions put in motion by CAFs that

impact the neoplastic epithelium, makes the targeting of these molecules and processes inefficient as a viable therapeutic strategy in cancer. However, the identification of the master transcriptional mechanisms whereby normal fibroblasts become CAFs will probably be less complex, more hierarchical and, therefore, more amenable to therapeutic intervention.

The role of the stromal activation in colorectal cancer (CRC) has been the focus of recent studies. This renewed interest in the CRC stroma stems from a series of recent transcriptomics approaches that better classify human CRC, and more accurately predict patient outcome than the mutational landscape of these tumors (Calon et al., 2015; Guinney et al., 2015). These analyses revealed that the patients with poorest prognosis are those included in the consensus molecular subtype 4 (CMS4) and in the CRC subtype 3 (CCS3) categories (Becht et al., 2016; De Sousa et al., 2013; Dienstmann et al., 2017; Guinney et al., 2015). These groups are characterized by a robust stromal response, and worse relapse-free and overall survival (De Sousa et al., 2013; Guinney et al., 2015). These correlative studies established that a highly mesenchymal/desmoplastic CRC is a hallmark of increased malignancy and resistance to therapy (Calon et al., 2015). Experimental evidence to support this concept has recently been obtained from studies in relevant genetically modified mouse models (Jackstadt et al., 2019; Liao et al., 2019; Nakanishi et al., 2018; Tauriello et al., 2018). The atypical protein kinase C (aPKC) family, which includes two members, PKCζ and PKCλ/ι (Griner and Kazanietz, 2007; Reina-Campos et al., 2019), have recently been shown to be critical players in the acquisition of the aggressive mesenchymal/desmoplastic phenotype in CRC (Nakanishi et al., 2018). Therefore, the arsenal of signaling molecules that regulate this process in the CRC epithelium is becoming progressively clear. However, the mechanisms in the fibroblasts that regulate the acquisition of the highly stromal phenotype in CMS4/CCS3 CRC patients still need to be fully clarified. Conceivably, the loss of PKCλ/ι and PKCζ that results in highly desmoplastic intestinal tumors when inactivated in the intestinal epithelium (Nakanishi et al., 2018), might also play an important and cell-autonomous role in the stroma of mesenchymal CRCs.

Here, we investigate the potential role of the aPKCs in the control of the desmoplastic and mesenchymal phenotype in CMS4 CRC tumors. We show that PKCζ, but not PKCλ/ι, expression is downregulated by TGFβ in the tumor stroma of human CSM4 tumors. The selective loss of PKCζ in colonic fibroblasts induces a CAF phenotype in vitro and promotes intestinal tumorigenesis in vivo, accompanied of a strong desmoplastic response. At the mechanistic level, the stromal loss of PKCζ activates SOX2 that drives the reprogramming of intestinal fibroblasts promoting a switch to a SFRP1/2-positive population. Our data demonstrate that the stromal SOX2-SFRP1/2 axis is critical for the development of the mesenchymal and immunosuppressed CMS4 microenvironment.

RESULTS

Human tumor stroma displays reduced expression of PKCζ

Bioinformatics analyses of human cancer datasets revealed that *PRKCZ* (gene encoding PKCζ) mRNA expression was reduced in the tumor stroma, as compared to normal stroma, in CRC and other cancers (Figure 1A). *PRKCZ* mRNA levels were also reduced in isolated

human CRC CAFs as compared to normal fibroblasts (Figure 1B). In contrast, the expression of *PRKCI* (gene encoding PKCλ/ι) mRNA was not different between normal and tumor stroma nor between NFs and CAFs in any of these datasets (Figures S1A and S1B). Co-immunostaining of PKCζ and the stroma markers vimentin or αSMA revealed the downregulation of PKCζ protein levels in the stroma of human colon tumors as compared to normal tissue (Figures 1C, 1D, S1C and S1D). We next immunostained PKCζ in the stroma of colonic polyps that were pathologically classified either as sessile serrated lesions (SSLs) or as tubular adenomas (TAs). Our analysis demonstrates that SSLs, which usually progress toward serrated CRC with stromal activation (De Sousa et al., 2013; Nakanishi et al., 2018), showed reduced PKCζ staining in the tumor stroma as compared to normal stroma, whereas no significant differences were found between the stroma of TA samples and their normal stroma (Figures 1E and 1F). We next stained a large cohort of 155 CRC samples, which showed that 47% of these cases were negative for PKCζ expression in the stroma (Figure 1G and Table S1). Stromal PKCζ protein levels in these samples negatively correlated with tumor invasion, lymph node metastasis, and TNM stage (Table S1). Among the patients who had undergone a resection of the primary tumors, Kaplan-Meier survival curves showed that the recurrence-free and overall survival of those with PKCζ-negative stroma were significantly worse than those with PKCζ-positive stroma (Figure 1H). Furthermore, univariate analysis of these patients revealed that the recurrence-free survival in this cohort negatively correlated not only with tumor invasion, lymph node metastasis, and lymphatic invasion, but also with stromal PKCζ levels (Figure S1E). Multivariable logistic regression analysis showed that PKCζ expression in the stroma was an independent predictive factor for the recurrence-free survival of CRC patients, as well as for lymph node metastasis (Figure S1E). To determine whether stromal PKCζ expression correlated with the CMS4 subtype, an immunohistochemistry-based classifier that can be employed to identify molecular colorectal cancer subtypes was applied to our TMA (Trinh et al., 2017). Interestingly, PKCζ expression in the stroma of these patients inversely correlated with the CMS4 subtype (Figures 1I and S1F). Collectively, these results demonstrate that the stromal expression of PKCζ negatively correlates with desmoplasia and tumor malignancy in CRC, which suggests that PKCζ plays a tumor suppressor role in the stroma. Notably, PKCζ protein levels in the epithelium of CRC patients also negatively correlated with tumor invasion (Table S1) and with worse recurrence-free and overall survival (Figure S1G). Like in the case of stroma PKCζ, its reduced levels in the epithelium were also associated with the CMS4 subtype (Figure S1H). Interestingly, there was a positive correlation between the loss of PKCζ in the stroma and in the epithelium (Figure S1I), which suggests a common mechanism regulating PKCζ expression in both tumor cellular compartments. Furthermore, GSEA showed an inverse correlation of *PRKCZ* mRNA levels with EMT and TGFβ signatures in human CRC stroma datasets (Figure S1J), in keeping with previous data on the reduced amount of *PRKCZ* in the CRC epithelium (Llado et al., 2015; Ma et al., 2013; Nakanishi et al., 2019; Shelton et al., 2018). Therefore, we hypothesized that TGFβ activation could lead to the transcriptional repression of *PRKCZ* in CRC.

To test this possibility, we used tumor organoids (MTOs) generated from mice with simultaneous mutations in *Apc*, *Trp53, Kras,* and *Tgfbr2,* which have been reported to conform the CMS4 phenotype (Tauriello et al., 2018) and produce high levels of TGFβ as

compared to normal organoids (Figure 1J). Incubation of colon fibroblasts (CFs) with conditioned medium (CM) from these MTO cultures resulted in the downregulation of *Prkcz* (Figures 1K and 1L). Importantly, treatment of CFs with increasing doses of TGFβ effectively downregulated *Prkcz* expression concomitant with an enhanced activation of the CAF marker *Acta2* (Figure 1M). Likewise, treatment of human APC mutant organoids with TGFβ also downregulated *PRKCZ* (Figure 1N). Interrogation of human datasets of several tumor types confirmed that *PRKCZ* expression was reduced upon TGFβ treatment (Figure S1K). Consistently, incubation of CFs with Galunisertib, a TGFβR inhibitor, upregulated *Prkcz* expression and blocks its downregulation by the MTO CM (Figures 1O-1Q). These results demonstrate that *Prkcz* is transcriptionally repressed by TGFβ.

The incubation of CFs with trichostatin A (TSA), an inhibitor of HDACs, abolished *Prkcz* repression by TGFβ, demonstrating the critical role of acetylation in the regulation of *Prkcz* expression (Figure 1R). Moreover, epigenomic analysis of the promoter of *PRKCZ* in normal epithelial crypts, as compared to CRC cells lines, revealed a selective loss of H3K27Ac, an epigenetic mark of active enhancer elements (Figure 1S). JASPAR analysis of the H3K27Ac peak in the *PRKCZ* promoter identified a SMAD3 motif adjacent to an E2F4 motif that constitutes a previously described TGFβ inhibitory element (TIE; Figure 1S). This element has been shown to be critical in mediating transcriptional repression by TGFβ (Chen et al., 2002; Kang et al., 2005; Lakshmi et al., 2017). In keeping with these results, GSEA using the C3 MSigDB collection of transcription factor signatures, demonstrated the inverse correlation of *PRKCZ* expression with many E2F signatures (Figure S1L). These results suggest a model whereby a TGFβ-mediated repression mechanism promotes the loss of PKCζ in CRC (Figure S1M).

PKCζ-deficient CFs have characteristics of CAF

To investigate the potential role of PKCζ in the induction of the CAF phenotype, we isolated colonic fibroblasts (CFs) either from wild-type (WT) or PKCζ-deficient (*Prkcz*$^{-/-}$) mice and their invasive capacity and ability to impact the function of colon cancer cells was determined. *Prkcz*$^{-/-}$ CFs stimulated the migration and invasion of CRC epithelial cells to levels higher than those induced by WT CFs (Figures 2A-2C). In contrast, PKCλ/ι-deficient CFs showed no effect on these two parameters (Figures S2A-S2C). *Prkcz*$^{-/-}$ CFs showed increased capacity to stimulate invasion of CRC epithelial cells also in 3-D organotypic cultures (Figures 2D-2F and S2D). *Prkcz*$^{-/-}$ CFs also enhanced the invasive potential of MTOs and promoted the generation of larger and more numerous MTOs than those co-cultured with WT CFs (Figures 2G-2I). MTOs cultured in the presence of *Prkcz*$^{-/-}$ CFs, but not with WT controls, can migrate outside the matrix and grow as spheroids (Figures 2J-2L). Also, *Prkcz*$^{-/-}$ CFs showed an increased contraction of collagen gels, a measure of their extracellular matrix remodeling capacity (ECM) (Calvo et al., 2013) (Figures 2M-2O). These data indicate that the loss of PKCζ in CFs upregulates collagenases and other metalloproteinases, which are an integral part of the CAF signature (Kalluri, 2016). As compared to WT controls, PKCζ-deficient CFs not only have higher mRNA amounts of *Acta2* (αSMA) and *Il-6*, but also of the metalloproteinase *Mmp9* (Figure 2P). Similar conclusions were obtained in experiments in which PKCζ was acutely KO by adeno-Cre transduction of *Prkcz*$^{f/f}$ CFs (Figures S2E-S2H). All these evidences demonstrate that PKCζ

deficiency in stromal CFs induced a CAF phenotype that can enhance cancer cell invasion and the generation of ECM.

PKCζ-deficient CFs promotes tumorigenesis *in vivo*

To determine the *in vivo* role of stromal PKCζ deficiency in intestinal cancer, we targeted fibroblasts with the fibroblast-specific protein 1 *Fsp1-Cre* mouse line (Bhowmick et al., 2004; Sahai et al., 2020). To confirm the cell specificity of the *Fsp1-Cre* mouse line in the intestine, we crossed these mice with the Rosa26R$^{CAG\text{-}tdTomato}$ reporter mouse line. Immunofluorescence (IF) analysis of colon samples confirmed the expression of Tomato^{+} cells in the stroma as revealed by co-staining with Vimentin, PDGFRβ and Collagen-I in more than 80 percent of double positive cells (Figures 3A-3C). In contrast, we found a complete lack of Tomato^{+} cells in the colon epithelium as shown by staining with the epithelial marker E-Cadherin, and a minimal residual co-staining of Tomato^{+} cells with CD45^{+} cells (Figures 3A-3C). These results established the specificity of this Cre-line for the colon stroma. Therefore, we next crossed *Prkcz*$^{f/f}$ mice with *Fsp1-Cre* mice (to generate *Prkcz*$^{f/f}$;*Fsp1-Cre*) in which PKCζ was selectively and efficiently deleted in colon fibroblasts as demonstrated by double IF staining of PKCζ and Vimentin (Figures 3D and 3E). Although *Prkcz*$^{f/f}$;*Fsp1-Cre* mice did not shown any phenotype under basal conditions (Figures S3A-S3G), when subjected to the azoxymethane (AOM)/DSS protocol of intestinal carcinogenesis (Figure 3F), *Prkcz*$^{f/f}$;*Fsp1-Cre* mice developed more and larger colonic polyps and had reduced weight gain than identically treated *Prkcz*$^{f/f}$ mice (Figures 3G, 3H and S3H). Masson Trichrome and Collagen-I staining demonstrated the highly desmoplastic nature of *Prkcz*$^{f/f}$;*Fsp1-Cre* tumors (Figures 3I and S3I). Colon tumors in the *Prkcz*$^{f/f}$;*Fsp1-Cre* mice displayed higher cell proliferation and reduced apoptosis, which underlies their increased tumorigenicity (Figures S3J and S3K). These results demonstrate that the loss of PKCζ in fibroblasts enhanced intestinal tumorigenesis in vivo associated with a robust desmoplastic response.

Supporting these observations, MTOs inoculated into the rectum of *Prkcz*$^{f/f}$;*Fsp1-Cre* mice gave bigger orthotopic tumors and larger number of metastases in several organs than those transplanted into *Prkcz*$^{f/f}$ mice (Figures 3J-3M). *Prkcz*$^{f/f}$;*Fsp1-Cre* tumors had a more abundant stroma than those implanted into *Prkcz*$^{f/f}$ mice, as determined by Masson Trichrome and αSMA staining (Figures 3N and 3O). We also generated a fibroblast-specific conditional PKCλ/ι KO mice by crossing *Prkci*$^{f/f}$ and *Fsp1-Cre* mice. In marked contrast with the role of PKCζ, fibroblast-specific PKCλ/ι deficiency does not affect orthotopic tumor size or metastatic potential of implanted MTOs (Figures S3L-S3N). To further establish the cell-autonomous role of PKCζ in CFs *in vivo,* MTOs were transplanted into the cecum of *Prkcz*$^{f/f}$ mice admixed with either WT or *Prkcz*$^{-/-}$ CFs (Figure 3P). Co-transplantation with PKCζ-deficient CFs enhanced MTOs tumorigenesis and increased metastasis incidence (Figures 3Q-3S), with higher proliferation and desmoplasia but reduced apoptosis than those co-transplanted with WT CFs (Figures 3T, S3O and S3P). Similar results were obtained with AKP organoids (Roper et al., 2017) (Figures S3Q-S3U). Therefore, our data demonstrate that *Prkcz*$^{-/-}$ CFs have a pro-tumorigenic CAF phenotype not only *in vitro* but also *in vivo*.

PKCζ-deficient CFs activate SOX2

GSEA and NextBio analyses showed that signatures characteristic of CAF activation were upregulated in *Prkcz*$^{-/-}$ CFs (Figures 4A and S4A-S4C). Importantly, genes differentially expressed in *Prkcz*$^{-/-}$ CFs significantly correlated with the transcriptomic profile of the CMS4 tumor subtype in human CRCs (Nakanishi et al., 2018) (Figure S4D). We mapped the open chromatin landscape of *Prkcz*$^{-/-}$ CFs by ATAC-Seq. Bioinformatics analysis of differentially accessible regions between the two genotypes revealed that *Prkcz*$^{-/-}$ CFs had an increase in open genomic regions located close to genes involved in ECM remodeling (Figure S4E), which is consistent with the CAF phenotype of the *Prkcz*$^{-/-}$ CFs. To identify the key TFs orchestrating the CAF characteristics of the *Prkcz*$^{-/-}$ CFs, we combined transcriptomic and chromatin accessibility data using the PageRank algorithm Taiji (Zhang et al., 2019) (Figure S4F). From this analysis, *Sox2, Prrx1* and *Prrx2* were identified as potential key driver TFs in *Prkcz*$^{-/-}$ CFs (Figure 4B). *Sox2* is a prime candidate for further research because it is a master regulator of lineage cell plasticity (Sarkar and Hochedlinger, 2013). *Prrx1* and *Prrx2* are known regulators of EMT (Lv et al., 2017; Ocana et al., 2012). Consistently, *Sox2* is dramatically upregulated in *Prkcz*$^{-/-}$ CFs but barely expressed in WT CFs (Figures S5G and S5H). CRISPR/Cas9-mediated inactivation of *Sox2* completely abrogated the upregulation of *Prrx1* and *Prrx2* in *Prkcz*$^{-/-}$ CFs, which establishes the role of *Sox2* as the "apical" TF in the induction of the CAF phenotype (Figures S4G and S4H). Ingenuity Pathway Analysis (IPA) of the ATAC-seq data also revealed *Sox2* as the top-ranked predicted upstream regulator (Figure 4C). Close inspection of the ATAC-Seq data demonstrated the increased accessibility of the *Sox2* promoter (Figure S5I). Furthermore, ChIP-PCR experiments demonstrated a decrease in occupancy of the repressive H3K27me3 mark and the increase in occupancy of the activating H3K4me3 mark in the *Sox2* promoter region in *Prkcz*$^{-/-}$ CFs, as compared to WT controls (Figure S4J). In agreement with *Sox2* being the apical regulator of CAF activation in *Prkcz*$^{-/-}$, we found an extensive enrichment of transcripts from genes harboring SOX2 DNA binding motifs among the mRNAs that are upregulated in *Prkcz*$^{-/-}$ CFs (Figures 4D and S4K). Co-staining with vimentin or αSMA showed positive nuclear levels of SOX2 in the stroma of human colon tumors as compared to normal tissue (Figures 4E, 4F, S4L and S4M). SOX2 expression in the stroma was associated with CRC T invasion and worse prognosis in recurrence-free survival (Figures 4G and 4H and Table S1). Moreover, there was a negative correlation between SOX2 and PKCζ expression in the stroma of this cohort of CRC human patients (Figure 4I), and a positive correlation of stromal SOX2 with the CMS4 subtype (Figure 4J). We also found increased expression of SOX2 in the stroma of tumors induced by AOM-DSS treatment in *Prkcz*$^{f/f}$;*Fsp1-Cre* mice as compared to those in *Prkcz*$^{f/f}$ mice (Figure 4K). The repression of SOX2 levels requires PKCζ's kinase activity (Figures 4L and 4M). Previous results suggested that PKCλ/ι promoted SOX2 activity by direct phosphorylation (Justilien et al., 2014). In vitro phosphorylation assays revealed that although SOX2 is a substrate for PKCλ/ι, it is not a substrate for PKCζ (Figure S5N). *Sox2* mRNA levels were shown to be reduced by miR200b/c and miR429 (Lu et al., 2014; Peng et al., 2012), while PKCζ deficiency resulted in the downregulation of these miRNAs in intestinal epithelial cells (Shelton et al., 2018). Therefore, we tested if PKCζ deficiency in CFs also resulted in reduced levels of these miRNAss, which would account for the upregulation of *Sox2* mRNA levels in these cells. Consistently, the levels of these miRNAs were reduced in *Prkcz*$^{-/-}$ CFs (Figure 4N).

Addition of a miR200b mimetic reduced SOX2 protein and mRNA levels in *Prkcz*$^{-/-}$ CFs cultures (Figures 4O and 4P), in agreement with the notion that PKCζ regulates *Sox2* levels through miR200.

Deletion of *Sox2* in *Prkcz*$^{-/-}$ CFs blocks CAF activation and tumorigenesis *in vitro* and *in vivo*

To investigate the importance of SOX2 expression for CAF induction in *Prkcz*$^{-/-}$ CFs, we carried out a transcriptomic profiling of *Prkcz*$^{-/-}$sg*Sox2* CFs. GSEA revealed that the loss of *Sox2* reverted the upregulation of the CAF signatures in *Prkcz*$^{-/-}$ CFs (Figures 5A-5D). q-PCR analysis of several representative genes validated this conclusion (Figure 5E). Deletion of *Sox2* also reverted the correlation between the loss of PKCζ and the CMS4 transcriptional signature in *Prkcz*$^{-/-}$ CFs (Figure S5A). While *Sox2* deficiency reduced the increased migration and invasion properties of *Prkcz*$^{-/-}$ CFs (Figure S5B), *Sox2* overexpression was sufficient to confer CAF characteristics to WT CFs (Figure S5C). To determine SOX2 function *in vivo,* we carried out a co-transplantation experiment in which MTOs were implanted in the cecum of WT mice along with WT, *Prkcz*$^{-/-}$ or *Prkcz*$^{-/-}$sg*Sox2* CFs (Figure 5F). Co-transplantation of *Prkcz*$^{-/-}$sg*Sox2* CFs with MTOs rescued the increased tumor size and incidence of metastasis promoted by *Prkcz*$^{-/-}$ CFs (Figures 5G-5I), which also correlated with reduced collagen deposition (Figure 5J). These results demonstrated that the ability of PKCζ deficiency in CFs to induce the CAF phenotype is mediated by the upregulation of SOX2, which acts as the master TF of this process.

PKCζ deficiency promotes the generation of a pro-tumorigenic CAF population through a SOX2-SFRP1/2 mechanism

To characterize the potential role of the PKCζ-SOX2 pathway in the generation of CAF heterogeneity in intestinal cancer *in vivo,* we performed single-cell transcriptomics of orthotopic tumors from MTOs implanted in the rectum of *Prkcz*$^{f/f}$;*Fsp1-Cre* or *Prkcz*$^{f/f}$ mice (Figures 6A and 6B). Three major cellular compartments were identified using known markers (Figure 6C). Re-clustering of the stromal compartment revealed its composition as four distinctive sub-clusters: fibroblasts, myofibroblasts, pericytes, and endothelial cells (Figures S6A and S6C). We next isolated the fibroblasts in silico and identified 4 distinct subpopulations (clusters 0-3) (Figure 6D). We found a switch in the populations of fibroblasts, with clusters 0 and 2 being the main ones in the tumor of *Prkcz*$^{f/f}$;*Fsp1-Cre* mice, while clusters 1 and 3 being the predominant subpopulations in the *Prkcz*$^{f/f}$ tumor (Figures 6D and 6E). *Acta2* was among the 5 top biomarkers of cluster 2, indicating its myofibroblastic/CAF phenotype, while *Col1a2* was among the 5 top gene biomarkers in cluster 0, which also included other collagen transcripts (Figure 6F and Table S2). The top biomarker in cluster 0 was *Sfrp2* (Figure 6F), whose homolog *Sfrp1* was also uniquely expressed in this cluster (Table S2). *Sfrp1* and *Sfrp2,* belong to the SFRP family of WNT signaling modulators and SFRP2 is secreted by fibroblasts to promote metastasis (Joesting et al., 2005; Kato et al., 2019; Kaur et al., 2016; Nguyen et al., 2019; Pelon et al., 2020; Sun et al., 2016). SFRP1 and SFRP2 are encoded by genes that harbor SOX2 binding sites in their promoters (Zhou et al., 2016). q-PCR analysis further established that *Sfrp1* and *Sfrp2* mRNAs were upregulated in *Prkcz*$^{-/-}$ CFs while reduced in *Prkcz*$^{-/-}$sg*Sox2* CFs (Figures 6G and S6D) and upregulated in SOX2-overexpressing PKCζ WT CFs (Figure S6E). ChIP-

qPCR demonstrated that the binding of SOX2 to the promoters of *Sfrp1* and *Sfrp2* was increased in *Prkcz*$^{-/-}$ CFs (Figure 6H). Immunostaining revealed that fibroblasts in the orthotopic tumors of *Prkcz*$^{f/f}$;*Fsp1-Cre* mice expressed abundant SFRP1 and SFRP2, as compared to *Prkcz*$^{f/f}$ controls (Figure 6I). Deletion of *Sfrp1* or *Sfrp2* suppressed the expression of mRNAs representative of CAF activity in *Prkcz*$^{-/-}$ CFs and inhibited the ability of these CFs to promote the migration and invasion of CRC epithelial cells (Figures S6F-S6L). Overexpression of *Sfrp1* or *Sfrp2* was sufficient to promote the upregulation of CAF markers in WT CFs (Figures S6M and S6N). These results demonstrated that *Sfrp1* and *Sfrp2* are direct targets of *Sox2* in *Prkcz*$^{-/-}$ CFs and have an essential role in the control of CAF activation. Transplantation experiments of MTO organoids with *Prkcz*$^{-/-}$sg*Sfrp2*, *Prkcz*$^{-/-}$, or sgCtr WT controls, showed that the loss of SRFP2 abolished the pro-tumorigenic and desmoplastic effects of PKCζ deficiency in CFs *in vivo* (Figures 6J-6M). Interrogation of a large TCGA cohort of human CRCs demonstrated a significant inverse correlation between *PRKCZ* and *SFRP1/2* mRNA levels (Figure S6O). GSEA established that the gene expression signature of Cluster 0 was highly enriched in patients of the CMS4 subtype as compared to the other subtypes in the TCGA cohort (Figure S6P). These data established the human relevance of the PKCζ-SOX2-SFRP1/2 axis as the driver of the CAF Cluster 0 in the most aggressive form of mesenchymal human CRC.

PKCζ-deficient CAFs drive enhanced β-catenin signaling in the tumor epithelium in an immunosuppressed microenvironment

Analysis of the scRNAseq data corresponding to the epithelial compartment revealed no alterations in the proportions of the different subpopulations between both genotypes (Figures S7A-S7C). However, in agreement with the more aggressive nature of these tumors, we found upregulation of signatures corresponding to EMT and TGFβ signaling in several clusters from the mutant mice (Figures 7A and S7D). Furthermore, consistent with the WNT modulatory role of *Sfrp1* and *Sfrp2,* we also identified the activation of the WNT signaling signature in all the epithelial clusters from the *Prkcz*$^{f/f}$;*Fsp1-Cre* mice (Figures 7A and S7D). Immunostaining for β-catenin of tumors from MTO organoids grown in *Prkcz*$^{f/f}$;*Fsp1-Cre* mice or from the AOM/DSS model in this same mouse line, further confirmed the activation of the WNT pathway *in vivo* in the epithelium of tumors with PKCζ-deficient stroma (Figures 7B, 7C, S7E and S7F). SFRP1/2 overexpression in CFs resulted in increased levels of WNT signaling transcripts, while their genetic inactivation abolished the upregulation of this pathway in *Prkcz*$^{-/-}$ CFs and in the epithelial compartment of the tumor (Figures 7D, 7E and S7G-S7I). Interestingly, recent data showed the activation of Notch signaling in the epithelium of CMS4 tumors (Jackstadt et al., 2019). Further inspection of the scRNAseq data showed the upregulation of a Notch signature in the tumor epithelium of *Prkcz*$^{f/f}$;*Fsp1-Cre* mice (Figures 7A and S7D). Immunostaining of cleaved Notch demonstrated increased Notch signaling activation in *Prkcz*$^{-/-}$*sgScr* tumors, which was reverted in *Prkcz*$^{-/-}$*sgSfrp2* tumors (Figures 7F and 7G). To further link the activation of these pathways by signals from the PKCζ-deficient CFs, CM from *Prkcz*$^{-/-}$*sgScr* CFs promoted the activation of the β-catenin and Notch pathways in MC38 cells, which was rescued by CM from *Prkcz*$^{-/-}$*sgSfrp2* CFs (Figures 7H and 7I).

Interestingly, GSVA analysis also showed the downregulation of signatures corresponding to allograft rejection and interferon pathways, a reflection of impaired immunosurveillance in the tumor epithelium of mice with a PKCζ-deficient stroma (Figures 7A and S7D). Consistently, nuclear p-Stat1 levels were reduced in tumors from PKCζ-deficient stroma, which was reverted upon *Sfrp2* deficiency (Figures 7J and 7K). This is in keeping with an immunosuppressive microenvironment, which in addition to increased desmoplasia and TGFβ signaling, is a salient feature of CMS4 tumors (Becht et al., 2016; Nakanishi et al., 2019; Roelands et al., 2017). Consistently, there was an impaired infiltration of $CD8^+$ T cells in tumors from PKCζ-deficient stroma, which was reverted by the simultaneous deletion of *Sfrp2* (Figures 7L-7O). Concomitant with the reduced content of $CD8^+$ T cells, there was an increased recruitment of neutrophils in the tumors of mice with a PKCζ-deficient stroma (Figure 7P). Further interrogation of the scRNAseq data demonstrated that these tumors also displayed reduced amounts of B cells and a switch in the neutrophil compartment towards a more immunosuppressive population (Figures 7Q, S7J and S7K), in agreement with the CMS4 characteristics of tumors with a PKCζ-deficient stroma. Immunostaining of these tumors confirmed the reduced recruitment of B cells (Figures 7R, 7S, S7L and S7M). scRNAseq analysis of the co-transplantation experiment (Figure 6J), confirmed the reduction in B cell content and the increase in neutrophils in *Prkcz*$^{-/-}$sg*Scr* tumors, which were rescued in *Prkcz*$^{-/-}$ sg*Sfrp2* tumors (Figures 7T, 7U and S7N). This B cell phenotype was also observed by immunostaining (Figures 7V and 7W). Interrogation of the epithelium of these tumors revealed a dramatic decrease of chemokines involved in B cell recruitment in tumors with a PKCζ-deficient stroma that was rescued upon simultaneous deletion of *Sfrp2* (Figure 7X).

DISCUSSION

Several signaling molecules in the tumor epithelium have been identified as central to the generation of the desmoplastic reaction in cancer. This response is characterized by a fibroblastic stroma, which contributes to the aggressiveness of the CMS4/CCS3 tumors (De Sousa et al., 2013; Guinney et al., 2015; Jackstadt et al., 2019; Liao et al., 2019; Mariathasan et al., 2018; Nakanishi et al., 2018; Tauriello et al., 2018). These molecules included the two aPKCs, whose levels are reduced in the tumor epithelium of human patients with this type of poor-prognosis CRC, and whose ablation in the mouse intestinal epithelium recapitulates the human mesenchymal serrated CRC phenotype (Nakanishi et al., 2018). Here, we have addressed the identification of the molecules in tumor fibroblasts that drive the generation of the CAF phenotype responsible for the enhanced malignancy of CSM4/CCS3 CRC. We found that stromal PKCζ is critically and negatively involved in this process by acting in a cell-autonomous manner. We show that PKCζ inhibition is instrumental for the induction of SOX2, which is necessary for the expression of SFRP1/2. According to our data, these two molecules are essential contributors to the CAF phenotype that drives higher levels of malignancy in intestinal tumors.

Our data also demonstrated that PKCζ deficiency in CFs controls the reprogramming of fibroblast heterogeneity in intestinal cancer, promoting a switch from two subpopulations that are less reactive and enriched in IFN-dependent transcripts, to two subpopulations that are more CAF and with distinctive signaling features among themselves. The most abundant

CAF population in the PKCζ-deficient stroma has *Sfrp2* as its top expresser. We demonstrate in this study that the *Sfrp* genes code for proteins that target the WNT signaling pathway both in the stroma, likely in an autocrine manner, and in the epithelium, which contributes to its increased tumorigenicity. Notably, a recent single-cell RNA sequencing study of human CRC reported a fibroblast population, termed S2, that resides in the proximity of the epithelial progenitor cells (Lee et al., 2020). This mesenchymal cell type that is characterized by high expression of WNT genes, is suggested to support the proliferation and function of progenitor cells. Interestingly, the S2 human colonic mesenchymal cell population shares a similar transcriptional identity with the *Sfrp1/2*-expressing CAF subpopulation (cluster 0) identified here as part of the PKCζ-deficient stroma. Therefore, our data lend mechanistic support to the notion that specific tumor fibroblasts serve to directly impact the growth of the tumor epithelium by promoting β-catenin and other progenitor signaling pathways in human CRC (Morral et al., 2020; Roulis et al., 2020; Vermeulen et al., 2010). Consistent with this model, there was an increased activation of β-catenin in the epithelial compartment of tumors with a PKCζ-deficient stroma, which was ablated by the inactivation of the *Sfrp2 gene* in PKCζ-deficient CAFs. SFRP1/2 also controlled the expression of Notch signaling in the tumor epithelium. Whether this is a direct effect of SFRP1/2 or mediated by Wnt remains to be determined. Therefore, a SOX2-SFRP1/2 axis activated by PKCζ deficiency in fibroblasts accounts for the generation of critical regulators of cell proliferation and invasion.

Interestingly, the loss of PKCζ in the stroma not only directly impacts tumor epithelial cell proliferation, but also recapitulates the induction of the CMS4/CCS3 immunosuppressive microenvironment. Thus, we show here that the epithelial cells in tumors deficient for PKCζ in the stroma displayed reduced antigen presentation and interferon pathway signatures. This is very interesting because our previous results demonstrated that PKCζ deficiency in the intestinal epithelium led to decreased interferon signaling and the consequent impaired immunosurveillance that allows intestinal tumors to initiate and progress to the generation of CMS4 CRC (Nakanishi et al., 2019; Nakanishi et al., 2018). Therefore, both the loss of PKCζ in the tumor epithelium and in the stroma results in enhanced immunoevasion through cell-autonomous and cell non-autonomous mechanisms, respectively. In addition, PKCζ-deficient CAFs not only contribute to an impaired immunosurveillance state in the tumor, but also drive the generation of an immunosuppressive tumor microenvironment by impacting the immune system. That is, we show here that a tumor PKCζ-deficient stroma is characterized by significant changes in immune cell populations, including neutrophils switched to a more immunosuppressive phenotype, as well as decreased number of B cells, both proposed hallmarks of the CMS4 microenvironment, and both phenotypes dependent on the SOX2-mediated induction of SFRP1/2 in the stroma.

The precise mechanism whereby PKCζ-deficient CAFs impact the immunological landscape of these tumors remains to be determined but the generation of TGFβ would likely play an important role. Thus, one of the signatures activated in the epithelium of tumors with a PKCζ-deficient stroma is “TGF_BETA_SIGNALING.” In this regard, previous data from our laboratory showed that PKCζ loss in intestinal epithelial cells gave rise to increased TGFβ signaling as part of a general activation program of stemness and EMT in the epithelium (Llado et al., 2015; Shelton et al., 2018). These observations,

together with the data shown here that PKCζ expression is downregulated by TGFβ through a previously unappreciated TGFβ inhibitory element in the PKCζ promoter, demonstrated the existence of a loop linking the epithelium and the stroma through a synergistic interaction between TGFβ and PKCζ. Therefore, PKCζ emerges as a central element in the epithelium-stromal crosstalk to promote epithelial cell proliferation and immunosuppression by impacting stemness in the epithelium and SOX2-driven SFRP1/2-expressing CAFs in the stroma. All these observations are relevant for human cancer because recurrence-free and overall survival of colorectal cancer patients negatively correlated with stromal PKCζ levels, while SOX2 expression in the stroma is associated with CRC T invasion and worse prognosis in recurrence-free survival.

STAR★ METHODS

RESOURCE AVAILABILITY

Lead Contact—Further information and requests for resources and reagents should be directed to and will be fulfilled by the Lead Contact, Jorge Moscat (jom4010@med.cornell.edu).

Materials Availability—Cell and mouse lines generated in this study are available from the Lead Contact upon request with a completed Materials Transfer Agreement.

Data and code Availability—The RNAseq, ATAC-seq, and scRNAseq datasets generated during this study have been deposited to the GEO repository on the NCBI website (Accession # GSE154843, GSE154857, GSE154852, GSE154863, and GSE157697). Original raw data have been deposited in Mendeley Data: https://doi.org/10.17632/5syy6gf4bw.1.

EXPERIMENTAL MODEL AND SUBJECT DETAILS

Mice—The *Prkcz*$^{-/-}$, *Prkcz*$^{f/f}$, *Prkci*$^{f/f}$ mice were previously described (Leitges et al., 2001; Llado et al., 2015; Nakanishi et al., 2016). *Prkcz*$^{f/f}$;*Fsp1-Cre* and *Prkci*$^{f/f}$;*Fsp1-Cre* mice were generated by breeding *Prkcz*$^{f/f}$ or *Prkci*$^{f/f}$ mice with *Fsp1-Cre* mice (Jackson Laboratory, stock number 012641). *Rosa26R*$^{CAG\text{-}tdTomato}$ mice were kindly provided by Alessandra Sacco (SBP Medical Discovery Institute). All mouse strains (except for NSG mouse) were generated in a C57BL/6 background and were born and maintained under pathogen-free conditions. Mice were sacrificed and small intestine, colon or other organs were collected for analysis. Animal handling and experimental procedures conformed to institutional guidelines and were approved by the SBP Medical Discovery Institute Institutional Animal Care and Use Committee. All genotyping was done by PCR. Age- and sex-matched mice were used for all experiments. Both male and females were used. The age and sex of mice used in each experiment are described under Figure legends.

Human samples—Paraffin-embedded tissue sections from samples were obtained from 80 patients during colonoscopy. Normal healthy colon samples (n = 20; male, n = 9, average age at diagnosis = 56 years old, age range 23-88 years old; female, n = 11, average age at diagnosis = 58, age range 29-81 years old), sessile serrated adenoma/polyp samples (n = 30;

male, n = 16, average age at diagnosis = 61 years old, age range 50-72 years old; female, n = 14, average age at diagnosis = 59, age range 46-75 years old), and tubular adenoma samples (n = 30; male, n = 23, average age at diagnosis = 65 years old, age range 39-83 years old; female, n = 7, average age at diagnosis = 53, age range 50-59 years old). Written informed consent was obtained from all patients with the protocol approved by the Ethics Committee of Scripps Green Hospital. PKCζ expression in stroma was evaluated by intensity (negative, weak, moderate or strong). For CRC samples, a total of 155 CRC patients (male, n = 79, average age at diagnosis = 64, age range 29-80; female, n = 76, average age at diagnosis = 67, age range 26-90) who had undergone a resection of the primary tumor at Osaka City University Hospital were analyzed. CRC tissues were obtained from each patient and none of the patients had undergone preoperative radiation or chemotherapy. This study was approved by the Osaka City University Ethics Committee and written informed consent was obtained from patients. De-identified human samples were sent to SBP Medical Discovery Institute and used for histological analyses. The study was approved by the IRB Committee of SBP Medical Discovery Institute.

Cell lines—WT and *Prkcz*$^{-/-}$ colon fibroblasts (CFs) were isolated from mouse colon (sex: female; age: 12 weeks-old). Mouse colon was surgically removed, placed on ice-cold HBSS, briefly washed and minced into 2- to 3-mm pieces. Then, tissue was washed eight times with HBSS by vigorous shaking and digested with 300 U/ml collagenase XI and 0.1 mg/ml dispase for 25 min at room temperature with gentle shaking followed by centrifugation at low speed for 10 min. The pellet was washed five times in DMEM with 2% sorbitol, and centrifuged 1-2 min at low speed. Cells were seeded into 6-well plates and cultured in DMEM with 10% FBS, insulin (10 μg/ml), transferrin (10 μg/ml), EGF (2 ng/ml) and gentamicin (10 μg/ml). *Prkci*$^{-/-}$ CFs were isolated from *Prkci*$^{f/f}$ mouse colon (sex: male; age: 8 weeks-old), and infected with Cre-recombinase adenovirus expressing green fluorescent protein (GFP). *Prkcz*$^{f/f}$ CFs were isolated from *Prkcz*$^{f/f}$ mouse colon (sex: male; 10 weeks-old). MC-38 cells (sex: female) were purchased from Kerafast. 293T cell line (sex: female) was obtained from ATCC. Colon fibroblasts, MC-38 and 293T cells were cultured in Dulbecco's modified Eagle's medium (DMEM) supplemented with 10% (vol/vol) fetal bovine serum (FBS), 1% glutamine and 1% penicillin-streptomycin in an atmosphere of 95% air and 5% CO2 at 37°C. MTOs were obtained from Dr. Eduard Batlle (Institute for Research in Biomedicine, Barcelona, Spain) and previously described (Tauriello et al., 2018). MTOs were cultured in advanced DMEM/F12 medium supplemented with 10 mM HEPES, Glutamax, B-27 (all Life Technologies), 50 ng/ml recombinant human EGF (Peprotech). Normal intestinal organoids were cultured in Advanced DMEM/F12 containing 10 mM HEPES, 1X Glutamax, 1X N2 supplement, 1X B27 supplement, 50 ng/ml EGF, 1000 ng/ml R-spondin 1, 100 ng/ml Noggin, and 10 μM Y-2763. Cultures were tested monthly for mycoplasma contamination.

METHOD DETAILS

Colitis-associated tumorigenesis—For AOM/DSS-induced inflammatory tumorigenesis, 8-10 weeks-old male mice received intraperitoneal injection of 10 mg/kg AOM (Sigma-Aldrich, St. Louis, MO, USA) before three cycles of DSS (molecular weight, 36,000–50,000; MP Biomedicals) administration. Tumor load was calculated by multiplying

tumor number and tumor diameter. All mice were maintained on food and water ad libitum and were age-matched and co-housed for all experiments.

Orthotopic injection of organoids—Mice were anaesthetized by isoflurane inhalation and placed in a supine position. A blunt-ended hemostat (Micro-Mosquito, No. 13010-12, Fine Science Tools) was inserted B1 cm into the anus, and the hemostat angled towards the mucosa and opened slightly such that a single mucosal fold could be clasped by closing the hemostat to the first notch. The hemostat was retracted from the anus, and the clasped exteriorized mucosa cleansed with povidone/iodine, rinsed with lactated ringer's solution and blotted dry. A 10-μl cell suspension of equivalent to 5×10^5 cells of MTOs admixed with 50% Matrigel (Corning) was directly injected into the colonic mucosae. After rehydrating the mucosa with phosphate-buffered saline (PBS), the hemostat was released and a blunt gavage needle used to re-insert the exteriorized colon, thus reversing the rectal prolapse. Mice were euthanized four weeks after injection and metastasis was scored macroscopically as well as histologically. To carry out orthotopic injections into cecum, mice were anesthetized with by isoflurane inhalation, exteriorizing their cecum by a laparotomy. An equivalent of 5×10^5 cells of MTOs or AKP organoids and 5×10^5 CFs in 11 μl was injected per mouse. Intercaecal injections were performed using a 31G needle under binocular guidance, with an approximate 30° angle and its tip introduced 5 mm into the cecal wall. The angular and slow rate of administration diminished resistance to the injection, limiting tissue damage and bleeding, ensuring the absence of cell reflux. After injection, the gut was returned to the abdominal cavity and closed. Mice were euthanized six weeks after injection and metastasis was scored macroscopically as well as histologically. Post-injection, all mice received analgesia (buprenorphine). Orthotopic tumor sizes were measured by caliper after mice were sacrificed.

Histology, immunohistochemistry and immunofluorescence—Intestines were isolated, rinsed in ice-cold PBS, fixed in 10% neutral buffered formalin overnight at 4 °C, dehydrated, and embedded in paraffin, followed by standard procedures for immunohistochemistry. For immunofluorescence, sections were incubated with Alexa-conjugated secondary antibodies (Life Technologies) and the samples examined with a Zeiss LSM 710 NLO Confocal Microscope. Antibodies used: rabbit anti-PKCζ (1:200, Abcam ab59364), rabbit anti-PKCζ (1:200, Abcam ab225554), rabbit anti-HTR2B (1:75, Sigma HPA012867), rabbit anti-FRMD6 (1:100, Abcam ab218209), rabbit anti-CDX2 (1:200, Novus Biologicals NB100-2136), rabbit anti-ZEB1 (1:500, Sigma HPA027524), mouse anti-Cytokeratin Pan Type I/II (1:500, Invitrogen MA5-13156), rabbit anti-RFP (1:200, Rockland 600-401-379), mouse anti-E-cadherin (1:100, BD Biosciences 610181), goat anti-Vimentin (1:50, Santa Cruz Biotechnology sc-7557), mouse anti-PDGFR beta (1:500, Abcam ab69506), mouse anti-Collagen I (1:300, Abcam ab88147), rabbit anti-Ki67 (ready-to-use, Thermo RM-9106-R7), rabbit anti-Chromogranin A (1:100, Abcam ab45179), rabbit anti-SOX9 (1:100, Sigma-Aldrich AB5535), rat anti-CD44 (1:800, BIO-RAD MCA4703), rat anti-CD45 (1:100, BD Biosciences 550539), rat anti-CD8 (1:200, BD Biosciences 550281), rat anti-CD45R (B220) (1:100, Thermo 17-0452-82), mouse anti-β-catenin (1:100, BD Biosciences 610153), mouse anti-αSMA (1:100, DAKO M0851), mouse anti-Sox2 (1:100, Santa Cruz Biotechnology sc-365823), rat anti-Sox2 (1:100, Invitrogen 14-9811-82), rabbit

anti-pStat1 (Cell Signaling Technology, 8826), rabbit anti-cleaved Notch1 (Cell Signaling Technology, 4147), mouse anti-HA-Tag (Cell Signaling Technology, 3724), rabbit anti-Sfrp1 (1:50, Abcam ab4193), rabbit anti-Sfrp2 (1:100, Abcam ab137560). Cell death was analyzed using the in-situ cell death detection kit, TMR red (Roche) for TUNEL. Masson's Trichrome staining was carried out following manufacturer's instructions (Sigma HT15-1KT). PKCζ and SOX2 expressions in human samples were evaluated by intensity of staining and percentage of stained cancer cells and stromal cells respectively: intensity was given scores 0-3 (0 = no, 1 = weak 2= moderate, 3 = intense), and the percentage of positive cells was given scores 0-4 (0 = 0%, 1 = 1%-30%, 2 = 31%-60%, 3 = 61%-80%, 4 = 81%-100%). The two scores were multiplied to obtain the final result of 0-12. Expressions were considered positive when scores were 6 or more (for PKCζ), 2 or more (for SOX2), and negative when scores were 5 or less (for PKCζ), 1 or less (for SOX2). Classification of CMS subtypes by immunohistochemistry was performed as previously described (Trinh et al., 2017). Slides were stained with anti-HTR2B (1:75; Sigma; HPA012867), anti-FRMD6 (1:100; Abcam; ab218209), anti-CDX2 (1:200; Novus Biologicals; NB100- 2136), anti-ZEB1 (1:500; Sigma; HPA027524), or anti-cytokeratin (AE1/AE3; 1:500; Thermo Scientific). After a secondary incubation with anti–rabbit-HRP or anti–mouse-HRP, staining was developed using DAB Chromogen (Dako), and slides were counterstained with hematoxylin. Slides were scored for CDX2, FRMD6, HTR2B, KER intensity and content, and ZEB1 nuclear content in epithelial cells blinded for CMS subtype. The online classifier (https://crcclassifier.shinyapps.io/app-Testing/) was used to separate the samples into CMS2/3 or CMS4 subtypes. Slides with a random forest probability of 60% were scored as CMS4.

Flow cytometry analysis—Flow cytometry experiments were performed using fresh tumors induced by orthotopic implantation. Briefly, fresh tumors were harvested, rinsed in cold PBS, minced into small pieces, incubated in HBSS with EDTA (5 mM) and digested with collagenase (0.05 mg/ml) for 30 min at 37 °C, followed by a discontinuous Percoll separation method (40 and 75%) to purify immune cells. The cells concentrated at the interface were collected and washed in cold PBS. Red blood cells were removed with lysing buffer (BD Pharm Lyse) and live cells were counted using Trypan blue and then saturated with mouse Fc Block (purified anti-mouse CD16/CD32; 1:50; clone 2.4G2; BD PharMingen) 30 min at 4 °C before incubating with specific dyed antibodies.

Cell culture experiments—For transient miRNA transfection experiments, 100 nM of the miRNA mimics for hsa-miR-200b-3p and the negative miRNA mimic transfection control were obtained from Invitrogen and were reverse transfected at the time of seeding using Lipofectamine RNAimax (Life Technologies). Transient overexpression of PKCζ-WT and PKCζ-Kinase death was achieved by transfection using X-tremeGENE HP transfection reagent (Roche). Transfected cells were examined 48 h after transfection. To knock down *Sfrp1, Sfrp2, Prrx1 and Prrx2,* small interfering RNAs (siRNAs) for *Sfrp1* (sc-39999), *Sfrp2* (sc-40001), *Prrx1* (sc-152531), *Prrx2* (sc-152532) and nontargeting siRNA (negative-siRNA) were purchased from Santa Cruz Biotechnology. Pooled siRNAs were reverse transfected at the time of seeding according to the manufacturer's protocol. To knock out *Sox2, Sfrp1* and *Sfrp2* in colonic fibroblasts, sgRNA targeting Sox2 exon1 (5'-CUCCAUCAUGUUAUACAUGC-3'), sgRNA targeting *Sfrp1* exon1 (5'-

UCGCCGAGCAACAUGGGCGU-3'), sgRNA targeting *Sfrp2* exon2 (5'-UUCACACACCUUGGGAGCUG -3') were purchased from Synthego and transduced into cells with recombinant Streptococcus pyogenes Cas9 protein (Truecut Cas9 Protein v2, Thermo). *Sox2, Sfrp1* and *Sfrp2* were knocked out using the Neon Transfection System 1 (Thermo) following the manufacturer's protocol and single clones were expanded and screened by protein immunoblotting.

Isolation of genome DNA and confirmation of CRISPR-cas9 Editing—Genomic DNA was isolated using QIAamp DNA Mini Kit following the manufacturer's protocol. PCR was carried out using AmpliTaq Gold® 360 Master Mix Protocol (Thermo Scientific), with oligonucleotides synthesized by Integrated DNA Technologies (IDT, Coralville, IA, United States) (Table S3). The amplification parameters were set at 95°C for 30 s, 56°C for 30 s, and 72°C for 30 s (35 cycles total) for *Sfrp1* and *Sfrp2* and set at 95°C for 30 s, 58°C for 30 s, and 72°C for 30 s (40 cycles total) for *Sox2*. DNA was purified using PCR cleanup kit (QIAGEN) and then used for direct Sanger sequencing by Eton Bioscience Inc (San Diego, CA).

Mammalian Lentiviral and Retroviral Transduction—pMXs-Sox2-IP, a gift from Shinya Yamanaka (Addgene plasmid #15919; http://n2t.net/addgene:15919; RRID:Addgene_15919) (Takahashi and Yamanaka, 2006), pLenti6.3/V5-DEST-SFRP1 (DNASU, HsCD00936572) and pLenti6.3/V5-DEST-SFRP2 (DNASU, HsCD00938859) were obtained from Addgene and DNASU. Actively growing HEK293T cells were co-transfected with pLenti-encoding plasmids, psPAX2 (Addgene, plasmid 12260) and pMD2.G (Addgene, plasmid 12259) packaging plasmids using X-tremeGENE transfection reagent. For retroviruses, pMXs-encoding plasmids were transfected into actively growing Phoenix cells with X-tremeGENE transfection reagent to produce viral particles, which were used to infect cells. Virus-containing supernatants were collected 48 and 72 h post-transfection and filtered to remove cells. Target cells were infected in the presence of 8 μg/ml polybrene. Cells were selected with puromycin after infection.

Migration and Invasion Assay—Colon cancer cells (MC-38 cells) were assayed for their ability to invade through a polyethylene terephthalate membrane inserts with 8 mm pores coated with extracellular matrix proteins in 24-well format (Matrigel Invasion Chambers, Corning). A total of 4 $x10^4$ (migration), 8 $x10^4$ (invasion) cells/well were seeded into the inner chamber in serum-free DMEM, and cells were challenged with conditioned media from fibroblasts of indicated genotype in the outer chamber. After 22 h of incubation at 37 °C, 5% CO_2, cells that invaded through the pores onto the bottom of the insert were fixed in cold methanol and stained with crystal violet.

Organotypic Cultures—Three-D air liquid organotypic culture was used to determine the role of CFs on cancer cell invasion. Gels were composed of one ml of a mixture of 1.75 volumes of Matrigel, 5.25 volumes of collagen type I, 1 volume of 1x DMEM, 1 volume of 10x DMEM, and 1 volume of filtered FBS (Valencia et al., 2014). The mixture was plated onto 24-well plates coated with diluted collagen type I. Gels were allowed to equilibrate with 1 ml of 1x DMEM overnight at 37°C. 5 x 10^5 MC-38 cells and 5 x 10^5 CFs were

seeded on top of the matrix. Alternatively, equivalent to 5 x 10^5 MTOs were first seeded with 5 x 10^5 CFs in 0.1ml of 70% BME. After 5 min, normal medium was added. Gel rafts were placed onto collagen-coated nylon sheets and lifted using a sterile supporting steel mesh to set up a raised air-liquid culture. Normal medium was changed in alternate days and organotypic cultures were allowed to grow for 14 days. Afterwards, organotypic gels were harvested, fixed in 10% neutral buffered formalin, bisected and embedded in paraffin. H&E stained sections were analyzed with a Zeiss light microscope supplemented with Axiovision40 software.

Direct co-culture assays—Mixture of MTOs (equivalent to 5 x 10^4) and 5 x 10^4 CFs was seeded in 24-well plates and normal medium was added 5 min after seeding. The total number of migrating MTOs was determined by counting the cells after 3 days using a light microscope.

ECM-remodeling assay—To assess force-mediated matrix remodeling, 5 x 10^5 CFs were embedded in 1 ml of collagen I/Matrigel and seeded in 24-well plates. Once the gel was set, cells were maintained in normal medium for colonic fibroblasts. Gel contraction was monitored daily by taking photographs of the gels.

Chromatin immunoprecipitation (ChIP) analysis—ChIP was performed using the ChIP-IT® Express Enzymatic Magnetic Chromatin Immunoprecipitation Kit and Enzymatic Shearing Kit (Cat. No. 53009 and 53035; Active Motif) following the manufacturer's protocol. Approximately 6 million cells and 5-10 μg antibody were used for each ChIP. Antibodies used were control IgG and antibody specific to H3K27me3 (Active motif, 39055), H3K4me3 (Active motif, 39159), and SOX2 (Cell Signaling Technology, 23064). The immunoprecipitated DNA was used in each PCR using promoter-specific primers described below. To evaluate site-specific enrichment, qPCR assays were carried out using the same amount of input DNA and immune-precipitated DNA. All primers used in ChIP assays are listed in Table S3.

RNA extraction and analysis—Total RNA from cultured CFs was extracted using TRIZOL reagent (Invitrogen), and purified by the RNeasy Mini Kit (QIAGEN), followed by DNase treatment. After quantification using a Nanodrop 1000 spectrophotometer (Thermo Scientific), RNA was either processed for RNA-seq or reverse-transcribed using random primers and MultiScribe Reverse Transcriptase (Applied Biosystems). Gene expression was analyzed by amplifying 20 ng of the complementary DNA using the CFX96 Real Time PCR Detection System with SYBR Green Master Mix (BioRad) and primers described in Table S3. The amplification parameters were set at 95°C for 30 s, 58°C for 30 s, and 72°C for 30 s (40 cycles total). Gene expression values for each sample were normalized to the 18S RNA.

Immunoblotting Analysis—Cells for protein analysis were lysed in RIPA buffer (20 mM Tris-HCl, 37 mM NaCl2, 2 mM EDTA, 1% Triton-X, 10% glycerol, 0.1% SDS, and 0.5% sodium deoxycholate) with phosphatase and protease inhibitors. Protein concentration in lysates were determined by using Protein Assay Kit (Bio-Rad). Cell extracts were denatured, subjected to SDS-PAGE, transferred to PVDF membranes (GE Healthcare). After blocking with 5% nonfat dry milk in Tris-buffered saline and 0.1% Tween (TBS-T), the membranes

were incubated with the specific antibodies (as listed in Key Resources Table) overnight at 4 °C. After 2 h incubation with the appropriate horseradish peroxidase-conjugated or fluorochrome-conjugated antibodies, the immune complexes were detected by chemiluminescence (Thermo Scientific) or Near-infrared fluorescence (LI-COR).

In Vitro Phosphorylation—For *in vitro* phosphorylation assay, recombinant SOX2 (Peprotech) was incubated at 30 ^{0}C for 60 min in kinase-assay buffer containing 175 mM Tris-HCl (pH 7.5), 50 mM MgCl2, 2.5 mM EGTA, 0.5 mM CaCl2 1 mM DTT, and 1 mM ATPγS (Sigma) in the presence or abcense of recombinant PKCλ/ι (Invitrogen) or PKCζ (Invitrogen). Briefly, after the phosphorylation reaction, PNBM (Abcam) and EDTA were added to a final concentration of 2.5 mM and 20 mM, respectively, and incubated for 1 h at room temperature. Immunoblotting detection was performed with anti-thiophosphate ester antibody (Abcam).

RNA-Seq library preparation and sequencing—For RNA-seq of CFs, total RNA was extracted from each 3 or 4 wells of CFs. RNA-seq studies were performed in the Genomics Core at SBP Medical Discovery Institute. Briefly, poly(A) RNA was isolated using the NEBNext® Poly(A) mRNA Magnetic Isolation Module and barcoded libraries were made using the NEBNext® Ultra™ Directional RNA Library Prep Kit for Illumina® (NEB, Ipswich MA). Libraries were pooled and single end sequenced (1X75) on the Illumina NextSeq 500 using the High output V2.5 kit (Illumina Inc., San Diego CA).

ATAC-Seq library preparation and sequencing—The cell pellet was resuspended in 50 µl lysis buffer and then spun down 500 × g for 10 min at 4 °C. The nuclei pellet was resuspended into 50 µl transposition reaction mixture containing Tn5 transposase from Nextera DNA Library Prep Kit (Illumina) and incubated at 37 °C for 30 min. Then the transposase-associated DNA was purified using MinElute PCR purification kit (QIAGEN). To amplify the library, the DNA was first amplified for 5 cycles using indexing primer from Nextera kit and NEBNext High-Fidelity 2X PCR master mix. To reduce the PCR amplification bias, 5 µl of amplified DNA after the first 5 cycles was used to do qPCR of 20 cycles to decide the number of cycles for the second round of PCR. Usually the maximum cycle of the second round of PCR is 5 cycles. Then the total amplified DNA was size selected to fragments less than 800 bp using SPRI beads. Quantification of the ATAC-seq library was done with QuBit. The size of the pooled library was examined by TapeStation. Barcoded ATAC-seq libraries were pooled and paired end sequenced (sX75) on the Illumina NextSeq 500 using the High output V2.5 kit (Illumina Inc., San Diego, CA).

10x library preparation and sequencing—Tumors were minced thoroughly and digested by 0.5 mg/ml Liberase TH (Sigma) for 30 minutes at 37°C. Dead cells were removed by Annexin V (STEMCELL technologies). scRNA-seq libraries were generated using the Chromium Single Cell 30 Reagent Kit v2 (10X Genomics). Cells were loaded onto the 10X Chromium Single Cell Platform (10X Genomics) at a concentration of 2,000 cells per µl (Single Cell 3′ library and Gel Bead Kit v.2) as described in the manufacturer's protocol (10x User Guide, Revision B). On average, approximately 8,000 cells were loaded. Generation of gel beads in emulsion (GEMs), barcoding, GEM-RT clean-up, complementary

DNA amplification and library construction were all performed as per the manufacturer's protocol. Individual sample quality was checked using a Bioanalyzer Tapestation (Agilent). Qubit was used for library quantification before pooling. The final library pool was sequenced on an Illumina NovaSeq6000 instrument using a S1 flow cell. Average cell recovery for the orthotopic in the Fsp1-cre mice was 23,576 cells, with a total of 47153 cells captured at a mean depth of 18712 reads per cell and 1224 mean genes per cell. Average cell recovery for the orthotopic in caecum was 15628 cells, with a total of 46886 cells captured at a mean depth of 18712 reads per cell and 1492 mean genes per cell.

3′RNA-seq preparation and sequencing—Total RNA was extracted using Quick-RNA MiniPrep kit (Zymo Research). Libraries were prepared from 200 ng of total RNA using the QuantSeq 3' mRNA-Seq Library Prep Kit FWD for Illumina from Lexogen, and optional UMIs (Vienna, Austria). Barcoded libraries were pooled, and single end sequenced (1X75) on the Illumina NextSeq 500 using the High output V2.5 kit (Illumina Inc., San Diego CA).

Bioinformatics Analysis—For prediction of Sox2 target genes, genome coordinates of the promoters of the differentially expressed genes detected by RNA-seq with a p val. < 0.05 were obtained from the USCS Table Browser. The resultant bed files were then converted to FASTA files using the tool Extract Genomic DNA in UseGalaxy.org. JASPAR^{2020} was used to obtain the DNA-binding motifs for Sox2, modeled as matrices. The tool FIMO (Find Individual Motif Occurrences) from The MEME Suite was used to scan the sequences in the FASTA format for occurrences of the Sox2 motifs. For RNA-Seq, sequencing Fastq files were uploaded to BaseSpace and processed with RNA-Seq Alignment App (Illumina) to obtain raw reads counts for each gene. GenePattern (https://genepattern.broadinstitute.org/gp/pages/index.jsf) was used to collapse gene matrix files (CollapseDataset module) or to assess the statistical significance of differential gene expression (ComparativeMarkerSelection module for microarray data and DESeq2 module for RNA-seq data). Heat-map representation of gene expression was generated using Morpheus (https://software.broadinstitute.org/morpheus/). Gene Set Enrichment Analysis (GSEA) was performed using GSEA 4.0 software (http://www.broadinstitute.org/gsea/index.jsp) with 1000 gene-set permutations using the gene-ranking metric T-test with the collections h.all.v7.0.symbols (Hallmarks), c5.all.v7.0.symbols (C5), or customized signatures. The "CMS4_UP" "and "CMS4_DOWN" signatures were generated based on a list of classifier genes of CMS4 subtype for human colorectal cancer (CRC) ("CMS4_UP", upregulated genes in CMS4 subtype, size = 28 ; "CMS4_DOWN", downregulated genes in CMS 4 subtype, size = 28 (Tauriello et al., 2018). Meta-analyses to identify overlapping and associated genes with publicly available data set were performed using the NextBioTM (Illumina) on-line search engine (www.nextbio.com). For 3'RNA-Seq, read data was processed with the BlueBee Genoics Platform (BlueBee, San Mateo, CA).For ATAC-Seq, FASTQ files from ATAC-seq reads were aligned to UCSC mm10 with Bowtie2 (bowtie2 --very-sensitive -x mm10 -1 FILE_merged_R1.fastq -2 FILE_merged_R2.fastq -X 1000 -p 12 | samtools view -u - | samtools sort - > FILE.bam). Peak calling was performed with MACS2 with a threshold of q<0.05. Peaks were annotated with ChipSeeker R package. PageRank analysis combining ATAC-Seq and RNA-Seq was performed with Taiji v0.5.0

(Zhang et al., 2019). Fold enrichment were uploaded to IPA to be analyzed using “Core Pathway Analysis”. Meta-analyses to identify overlapping and associated genes with publicly available data set were performed using the NextBioTM (Illumina) on-line search engine (www.nextbio.com). For scRNA-seq, raw sequence reads were quality-checked using FastQC software. The Cell Ranger version 2.1.1 software suite from 10X Genomics (https://support.10xgenomics.com/single-cell-gene-expression/software/downloads/latest) was used to process, align and summarize unique molecular identifier (UMI) counts against the mouse mm10 assembly reference genome analysis set, obtained from the University of California Santa Cruz (UCSC). Raw, unfiltered count matrices were imported into R for further processing. Raw UMI count matrices were filtered using the Seurat v 3.0 R package (Butler et al., 2018) to remove: barcodes with very low (empty wells) and very high (probably doublets) total UMI counts; matrices for which a high percentage of UMIs originated from mitochondrial features (more than 20%); and matrices for which fewer than 250 genes were expressed. Clustering was performed as follows. The percentage of mitochondrial features was considered to be a source of unwanted variation and was regressed out using the Seurat package. Dimensionality reduction was performed by principal component analysis and UMAP embedding with resolution 0.5. Cluster gene markers and differentially expressed genes between groups in each cluster were detected using the Wilcoxon Rank Sum test.

Bioinformatics Analysis of clinical data—Data for TCGA-CORAD was accessed through cBioportal (http://www.cbioportal.org/index.do). Raw gene expression data CRC patient datasets (GSE35602, GSE83591, GSE22863, GSE70468 and GSE46824) were directly accessed through the GEO website (NCBI). Levels of *PRKCZ, PRKCI, SOX2, SFRP1* and *SFRP2* gene expression were converted to z-scores and differential expression was assessed by t test comparisons. The “Biomarkers_Cluster0” signature was generated based on a list of upregulated genes of Cluster0 (“Biomarkers_Cluster0”, upregulated genes in Cluster0, size = 71) (Table S2).

QUANTIFICATION AND STATISTICAL ANALYSIS

All the statistical tests are justified for every figure. All samples represent biological replicates. Data are presented as the mean ± SEM. Statistical analysis was performed using GraphPad Prism 8 or the SPSS software program (SPSS Japan). Significant differences between groups were determined using a Student’s t test (two-tailed) when the data met the normal distribution tested by D’Agostino test. If the data did not meet this test, a Mann-Whitney test was used. Differences in Kaplan Meier plots were analyzed by Log-Rank (Mantel-Cox) test. The chi-square test or Fisher’s exact was used to determine the significance of differences between covariates. The Cox proportional hazard regression model was employed to estimate univariate and multivariate hazards ratio (HR) and 95% confidence interval (CI). Differences in staining for human adenoma samples were analyzed by performing ANOVA multiple comparisons (Kruskal-Wallis test). Logistic regression analysis was employed to estimate univariate and multivariate odds ratio and 95% confidence interval (CI). Values of $p < 0.05$ were considered as significantly different.

Supplementary Material

Refer to Web version on PubMed Central for supplementary material.

ACKNOWLEDGEMENTS

Research was supported by grants by NCI and NIDDK of the National Institutes of Health under awards numbers: R01CA207177, R01DK108743, R01CA211794 to J.M; and R01CA218254 and R01CA246765 to M.T.D.-M. The content is solely the responsibility of the authors and does not necessarily represent the official views of the National Institutes of Health. H.K. was supported by the Japan Society for Promotion of Science Postdoctoral Fellowship for Research Abroad and Research Fellowship supported by The Uehara Memorial Foundation. We thank the personnel of the Histology, Cell Imaging, Flow Cytometry, Genomics, Animal Facility, and Viral Vectors Shared Resources at SBP Medical Discovery Institute for technical assistance.

REFERENCES

Becht E, de Reynies A, Giraldo NA, Pilati C, Buttard B, Lacroix L, Selves J, Sautes-Fridman C, Laurent-Puig P, and Fridman WH (2016). Immune and Stromal Classification of Colorectal Cancer Is Associated with Molecular Subtypes and Relevant for Precision Immunotherapy. Clin Cancer Res 22, 4057–4066. [PubMed: 26994146]

Bhowmick NA, Chytil A, Plieth D, Gorska AE, Dumont N, Shappell S, Washington MK, Neilson EG, and Moses HL (2004). TGF-beta signaling in fibroblasts modulates the oncogenic potential of adjacent epithelia. Science 303, 848–851. [PubMed: 14764882]

Butler A, Hoffman P, Smibert P, Papalexi E, and Satija R (2018). Integrating single-cell transcriptomic data across different conditions, technologies, and species. Nat Biotechnol 36, 411–420. [PubMed: 29608179]

Calon A, Lonardo E, Berenguer-Llergo A, Espinet E, Hernando-Momblona X, Iglesias M, Sevillano M, Palomo-Ponce S, Tauriello DV, Byrom D, et al. (2015). Stromal gene expression defines poor-prognosis subtypes in colorectal cancer. Nat Genet 47, 320–329. [PubMed: 25706628]

Calvo F, Ege N, Grande-Garcia A, Hooper S, Jenkins RP, Chaudhry SI, Harrington K, Williamson P, Moeendarbary E, Charras G, and Sahai E (2013). Mechanotransduction and YAP-dependent matrix remodelling is required for the generation and maintenance of cancer-associated fibroblasts. Nat Cell Biol 15, 637–646. [PubMed: 23708000]

Chen CR, Kang Y, Siegel PM, and Massague J (2002). E2F4/5 and p107 as Smad cofactors linking the TGFbeta receptor to c-myc repression. Cell 110, 19–32. [PubMed: 12150994]

De Jaeghere EA, Denys HG, and De Wever O (2019). Fibroblasts Fuel Immune Escape in the Tumor Microenvironment. Trends Cancer 5, 704–723. [PubMed: 31735289]

De Sousa EMF, Wang X, Jansen M, Fessler E, Trinh A, de Rooij LP, de Jong JH, de Boer OJ, van Leersum R, Bijlsma MF, et al. (2013). Poor-prognosis colon cancer is defined by a molecularly distinct subtype and develops from serrated precursor lesions. Nat Med 19, 614–618. [PubMed: 23584090]

Dienstmann R, Vermeulen L, Guinney J, Kopetz S, Tejpar S, and Tabernero J (2017). Consensus molecular subtypes and the evolution of precision medicine in colorectal cancer. Nat Rev Cancer 17, 79–92. [PubMed: 28050011]

Griner EM, and Kazanietz MG (2007). Protein kinase C and other diacylglycerol effectors in cancer. Nat Rev Cancer 7, 281–294. [PubMed: 17384583]

Guinney J, Dienstmann R, Wang X, de Reynies A, Schlicker A, Soneson C, Marisa L, Roepman P, Nyamundanda G, Angelino P, et al. (2015). The consensus molecular subtypes of colorectal cancer. Nat Med 21, 1350–1356. [PubMed: 26457759]

Hanahan D, and Weinberg RA (2011). Hallmarks of cancer: the next generation. Cell 144, 646–674. [PubMed: 21376230]

Jackstadt R, van Hooff SR, Leach JD, Cortes-Lavaud X, Lohuis JO, Ridgway RA, Wouters VM, Roper J, Kendall TJ, Roxburgh CS, et al. (2019). Epithelial NOTCH Signaling Rewires the Tumor Microenvironment of Colorectal Cancer to Drive Poor-Prognosis Subtypes and Metastasis. Cancer Cell 36, 319–336 e317. [PubMed: 31526760]

Joesting MS, Perrin S, Elenbaas B, Fawell SE, Rubin JS, Franco OE, Hayward SW, Cunha GR, and Marker PC (2005). Identification of SFRP1 as a candidate mediator of stromal-to-epithelial signaling in prostate cancer. Cancer Res 65, 10423–10430. [PubMed: 16288033]

Justilien V, Walsh MP, Ali SA, Thompson EA, Murray NR, and Fields AP (2014). The PRKCI and SOX2 oncogenes are coamplified and cooperate to activate Hedgehog signaling in lung squamous cell carcinoma. Cancer Cell 25, 139–151. [PubMed: 24525231]

Kalluri R (2016). The biology and function of fibroblasts in cancer. Nat Rev Cancer 16, 582–598. [PubMed: 27550820]

Kang JS, Alliston T, Delston R, and Derynck R (2005). Repression of Runx2 function by TGF-beta through recruitment of class II histone deacetylases by Smad3. EMBO J 24, 2543–2555. [PubMed: 15990875]

Kato M, Placencio-Hickok VR, Madhav A, Haldar S, Tripathi M, Billet S, Mishra R, Smith B, Rohena-Rivera K, Agarwal P, et al. (2019). Heterogeneous cancer-associated fibroblast population potentiates neuroendocrine differentiation and castrate resistance in a CD105-dependent manner. Oncogene 38, 716–730. [PubMed: 30177832]

Kaur A, Webster MR, Marchbank K, Behera R, Ndoye A, Kugel CH 3rd, Dang VM, Appleton J, O'Connell MP, Cheng P, et al. (2016). sFRP2 in the aged microenvironment drives melanoma metastasis and therapy resistance. Nature 532, 250–254. [PubMed: 27042933]

Lakshmi SP, Reddy AT, and Reddy RC (2017). Transforming growth factor beta suppresses peroxisome proliferator-activated receptor gamma expression via both SMAD binding and novel TGF-beta inhibitory elements. Biochem J 474, 1531–1546. [PubMed: 28100650]

Lee HO, Hong Y, Etlioglu HE, Cho YB, Pomella V, Van den Bosch B, Vanhecke J, Verbandt S, Hong H, Min JW, et al. (2020). Lineage-dependent gene expression programs influence the immune landscape of colorectal cancer. Nat Genet 52, 594–603. [PubMed: 32451460]

Leitges M, Sanz L, Martin P, Duran A, Braun U, Garcia JF, Camacho F, Diaz-Meco MT, Rennert PD, and Moscat J (2001). Targeted disruption of the zetaPKC gene results in the impairment of the NF-kappaB pathway. Mol Cell 8, 771–780. [PubMed: 11684013]

Liao W, Overman MJ, Boutin AT, Shang X, Zhao D, Dey P, Li J, Wang G, Lan Z, Li J, et al. (2019). KRAS-IRF2 Axis Drives Immune Suppression and Immune Therapy Resistance in Colorectal Cancer. Cancer Cell 35, 559–572 e557. [PubMed: 30905761]

Linares JF, Cordes T, Duran A, Reina-Campos M, Valencia T, Ahn CS, Castilla EA, Moscat J, Metallo CM, and Diaz-Meco MT (2017). ATF4-Induced Metabolic Reprograming Is a Synthetic Vulnerability of the p62-Deficient Tumor Stroma. Cell Metab 26, 817–829 e816. [PubMed: 28988820]

Llado V, Nakanishi Y, Duran A, Reina-Campos M, Shelton PM, Linares JF, Yajima T, Campos A, Aza-Blanc P, Leitges M, et al. (2015). Repression of Intestinal Stem Cell Function and Tumorigenesis through Direct Phosphorylation of beta-Catenin and Yap by PKCzeta. Cell Rep 10, 740–754. [PubMed: 25660024]

Lu YX, Yuan L, Xue XL, Zhou M, Liu Y, Zhang C, Li JP, Zheng L, Hong M, and Li XN (2014). Regulation of colorectal carcinoma stemness, growth, and metastasis by an miR-200c-Sox2-negative feedback loop mechanism. Clin Cancer Res 20, 2631–2642. [PubMed: 24658157]

Lv ZD, Wang HB, Liu XP, Jin LY, Shen RW, Wang XG, Kong B, Qu HL, Li FN, and Yang QF (2017). Silencing of Prrx2 Inhibits the Invasion and Metastasis of Breast Cancer both In Vitro and In Vivo by Reversing Epithelial-Mesenchymal Transition. Cell Physiol Biochem 42, 1847–1856. [PubMed: 28750408]

Ma L, Tao Y, Duran A, Llado V, Galvez A, Barger JF, Castilla EA, Chen J, Yajima T, Porollo A, et al. (2013). Control of nutrient stress-induced metabolic reprogramming by PKCzeta in tumorigenesis. Cell 152, 599–611. [PubMed: 23374352]

Mariathasan S, Turley SJ, Nickles D, Castiglioni A, Yuen K, Wang Y, Kadel EE III, Koeppen H, Astarita JL, Cubas R, et al. (2018). TGFbeta attenuates tumour response to PD-L1 blockade by contributing to exclusion of T cells. Nature 554, 544–548. [PubMed: 29443960]

Morral C, Stanisavljevic J, Hernando-Momblona X, Mereu E, Alvarez-Varela A, Cortina C, Stork D, Slebe F, Turon G, Whissell G, et al. (2020). Zonation of Ribosomal DNA Transcription Defines a Stem Cell Hierarchy in Colorectal Cancer. Cell Stem Cell 26, 845–861 e812. [PubMed: 32396863]

Nakanishi Y, Diaz-Meco MT, and Moscat J (2019). Serrated Colorectal Cancer: The Road Less Travelled? Trends Cancer 5, 742–754. [PubMed: 31735291]

Nakanishi Y, Duran A, L'Hermitte A, Shelton PM, Nakanishi N, Reina-Campos M, Huang J, Soldevila F, Baaten BJG, Tauriello DVF, et al. (2018). Simultaneous Loss of Both Atypical Protein Kinase C Genes in the Intestinal Epithelium Drives Serrated Intestinal Cancer by Impairing Immunosurveillance. Immunity 49, 1132–1147 e1137. [PubMed: 30552022]

Nakanishi Y, Reina-Campos M, Nakanishi N, Llado V, Elmen L, Peterson S, Campos A, De SK, Leitges M, Ikeuchi H, et al. (2016). Control of Paneth Cell Fate, Intestinal Inflammation, and Tumorigenesis by PKClambda/iota. Cell Rep 16, 3297–3310. [PubMed: 27653691]

Nguyen EV, Pereira BA, Lawrence MG, Ma X, Rebello RJ, Chan H, Niranjan B, Wu Y, Ellem S, Guan X, et al. (2019). Proteomic Profiling of Human Prostate Cancer-associated Fibroblasts (CAF) Reveals LOXL2-dependent Regulation of the Tumor Microenvironment. Mol Cell Proteomics 18, 1410–1427. [PubMed: 31061140]

Ocana OH, Corcoles R, Fabra A, Moreno-Bueno G, Acloque H, Vega S, Barrallo-Gimeno A, Cano A, and Nieto MA (2012). Metastatic colonization requires the repression of the epithelial-mesenchymal transition inducer Prrx1. Cancer Cell 22, 709–724. [PubMed: 23201163]

Pelon F, Bourachot B, Kieffer Y, Magagna I, Mermet-Meillon F, Bonnet I, Costa A, Givel AM, Attieh Y, Barbazan J, et al. (2020). Cancer-associated fibroblast heterogeneity in axillary lymph nodes drives metastases in breast cancer through complementary mechanisms. Nat Commun 11, 404. [PubMed: 31964880]

Peng C, Li N, Ng YK, Zhang J, Meier F, Theis FJ, Merkenschlager M, Chen W, Wurst W, and Prakash N (2012). A unilateral negative feedback loop between miR-200 microRNAs and Sox2/E2F3 controls neural progenitor cell-cycle exit and differentiation. J Neurosci 32, 13292–13308. [PubMed: 22993445]

Quail DF, and Joyce JA (2013). Microenvironmental regulation of tumor progression and metastasis. Nat Med 19, 1423–1437. [PubMed: 24202395]

Reina-Campos M, Diaz-Meco MT, and Moscat J (2019). The Dual Roles of the Atypical Protein Kinase Cs in Cancer. Cancer Cell 36, 218–235. [PubMed: 31474570]

Roelands J, Kuppen PJK, Vermeulen L, Maccalli C, Decock J, Wang E, Marincola FM, Bedognetti D, and Hendrickx W (2017). Immunogenomic Classification of Colorectal Cancer and Therapeutic Implications. Int J Mol Sci 18.

Roper J, Tammela T, Cetinbas NM, Akkad A, Roghanian A, Rickelt S, Almeqdadi M, Wu K, Oberli MA, Sanchez-Rivera FJ, et al. (2017). In vivo genome editing and organoid transplantation models of colorectal cancer and metastasis. Nat Biotechnol 35, 569–576. [PubMed: 28459449]

Roulis M, Kaklamanos A, Schernthanner M, Bielecki P, Zhao J, Kaffe E, Frommelt LS, Qu R, Knapp MS, Henriques A, et al. (2020). Paracrine orchestration of intestinal tumorigenesis by a mesenchymal niche. Nature 580, 524–529. [PubMed: 32322056]

Sahai E, Astsaturov I, Cukierman E, DeNardo DG, Egeblad M, Evans RM, Fearon D, Greten FR, Hingorani SR, Hunter T, et al. (2020). A framework for advancing our understanding of cancer-associated fibroblasts. Nat Rev Cancer 20, 174–186. [PubMed: 31980749]

Sarkar A, and Hochedlinger K (2013). The sox family of transcription factors: versatile regulators of stem and progenitor cell fate. Cell Stem Cell 12, 15–30. [PubMed: 23290134]

Shelton PM, Duran A, Nakanishi Y, Reina-Campos M, Kasashima H, Llado V, Ma L, Campos A, Garcia-Olmo D, Garcia-Arranz M, et al. (2018). The Secretion of miR-200s by a PKCzeta/ADAR2 Signaling Axis Promotes Liver Metastasis in Colorectal Cancer. Cell Rep 23, 1178–1191. [PubMed: 29694894]

Sousa CM, Biancur DE, Wang X, Halbrook CJ, Sherman MH, Zhang L, Kremer D, Hwang RF, Witkiewicz AK, Ying H, et al. (2016). Pancreatic stellate cells support tumour metabolism through autophagic alanine secretion. Nature 536, 479–483. [PubMed: 27509858]

Sun Y, Zhu D, Chen F, Qian M, Wei H, Chen W, and Xu J (2016). SFRP2 augments WNT16B signaling to promote therapeutic resistance in the damaged tumor microenvironment. Oncogene 35, 4321–4334. [PubMed: 26751775]

Takahashi K, and Yamanaka S (2006). Induction of pluripotent stem cells from mouse embryonic and adult fibroblast cultures by defined factors. Cell 126, 663–676. [PubMed: 16904174]

Tauriello DVF, Palomo-Ponce S, Stork D, Berenguer-Llergo A, Badia-Ramentol J, Iglesias M, Sevillano M, Ibiza S, Canellas A, Hernando-Momblona X, et al. (2018). TGFbeta drives immune evasion in genetically reconstituted colon cancer metastasis. Nature 554, 538–543. [PubMed: 29443964]

Trinh A, Trumpi K, De Sousa EMF, Wang X, de Jong JH, Fessler E, Kuppen PJ, Reimers MS, Swets M, Koopman M, et al. (2017). Practical and Robust Identification of Molecular Subtypes in Colorectal Cancer by Immunohistochemistry. Clin Cancer Res 23, 387–398. [PubMed: 27459899]

Valencia T, Kim JY, Abu-Baker S, Moscat-Pardos J, Ahn CS, Reina-Campos M, Duran A, Castilla EA, Metallo CM, Diaz-Meco MT, and Moscat J (2014). Metabolic reprogramming of stromal fibroblasts through p62-mTORC1 signaling promotes inflammation and tumorigenesis. Cancer Cell 26, 121–135. [PubMed: 25002027]

Vermeulen L, De Sousa EMF, van der Heijden M, Cameron K, de Jong JH, Borovski T, Tuynman JB, Todaro M, Merz C, Rodermond H, et al. (2010). Wnt activity defines colon cancer stem cells and is regulated by the microenvironment. Nat Cell Biol 12, 468–476. [PubMed: 20418870]

Zhang K, Wang M, Zhao Y, and Wang W (2019). Taiji: System-level identification of key transcription factors reveals transcriptional waves in mouse embryonic development. Sci Adv 5, eaav3262. [PubMed: 30944857]

Zhou C, Yang X, Sun Y, Yu H, Zhang Y, and Jin Y (2016). Comprehensive profiling reveals mechanisms of SOX2-mediated cell fate specification in human ESCs and NPCs. Cell Res 26, 171–189. [PubMed: 26809499]

Highlights

- PKCζ is lost in the stroma of poor-prognosis mesenchymal human CMS4 CRC
- Stromal loss of PKCζ upregulates SOX2 to promote the CAF phenotype
- Selective deletion of PKCζ in fibroblast activates the SOX2/SFRP1/2 axis in vivo
- Stromal SOX2 negatively correlates with PKCζ and predicts poor survival in CRC

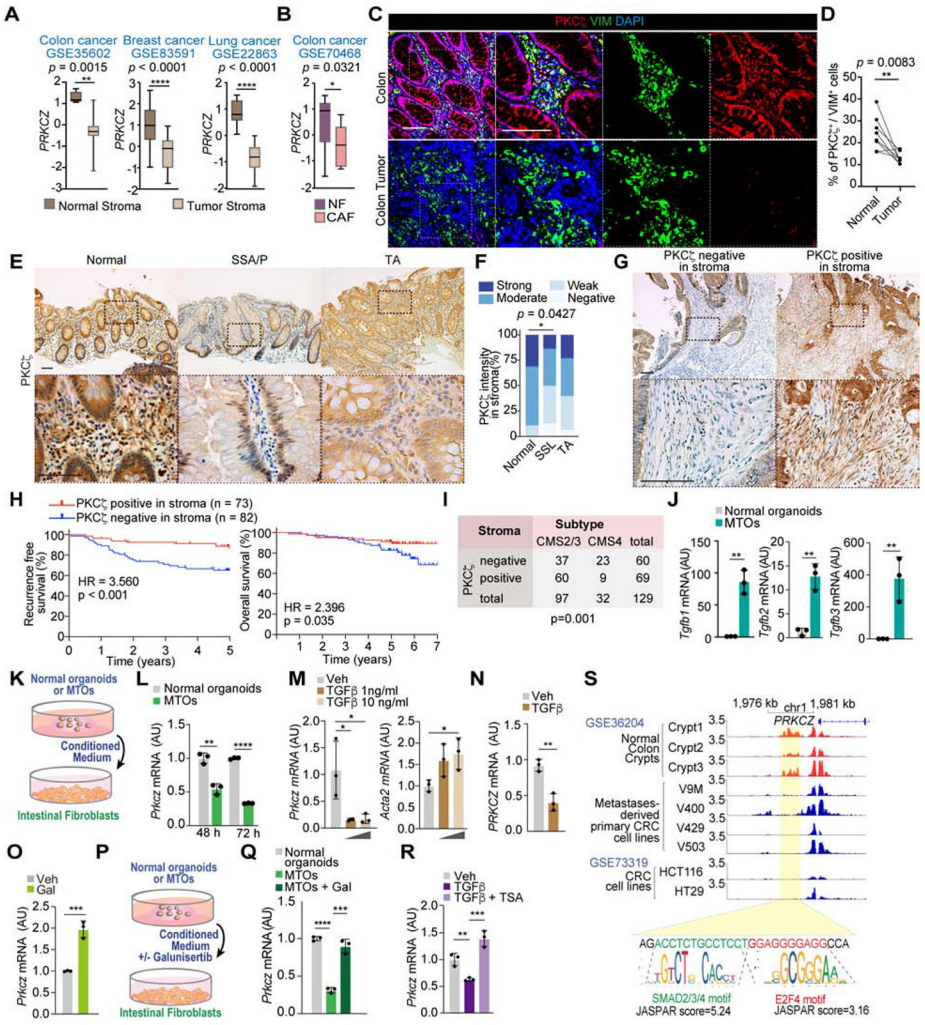

Figure 1. PKCζ expression is reduced in the stroma of human colorectal cancer

(A) *PRKCZ* mRNA levels in stroma of human cancer samples. Data were collected from GSE35602 (CRC, n = 17), GSE83591 (breast cancer, n = 53), and GSE22863 (lung cancer, n = 30).

(B) *PRKCZ* mRNA levels in isolated fibroblasts of colon cancer in dataset GSE70468 (n = 14). NF: normal fibroblasts; CAF: cancer associated fibroblasts.

(C and D) PKCζ staining (red) with Vimentin (green) (C) and quantification (D) in human CRC samples and normal counterparts (n = 8, paired). Scale bars, 50 μm.

(E and F) Stromal PKCζ immunohistochemistry (E) and quantification (F) of human normal colon, *n* = 20, sessile serrated adenoma/polyps (SSA/Ps; n = 30), and tubular adenomas (TAs; n = 30). Scale bars, 50 μm.

(G and H) Low PKCζ expression in stroma is a predictor of aggressive CRC and poor survival. PKCζ staining in a human cohort of CRC samples (n = 155) (G). Kaplan-Meier curve for 5-year recurrence-free survival and 7-year overall survival of CRC patients according to PKCζ expression (H).

(I) Correlation between PKCζ expression in CRC stroma and CMS subtypes (n = 129).

(J) *Tgfb1, Tgfb2 and Tgfb3* mRNA levels of normal intestinal organoids and MTOs (*n* = 3).

(K and L) *Prkcz* mRNA levels of CFs stimulated by conditioned medium (CM) of MTOs for 48 or 72 h (n = 3). Schematic representation (K) and qPCR (K).
(M) *Prkcz* and *Acta2* mRNA levels of CFs with TGFβ stimulation for 48 h (n = 3).
(N) *PRKCZ* mRNA levels in APC-KO human intestine organoids treated for 24 h with 0.5 μM TGFβ (GSE145308).
(O) *Prkcz* mRNA levels of CFs with Galunisertib (Gal) treatment for 48 h (n = 3, 10 μM).
(P and Q) *Prkcz* mRNA levels of CFs stimulated by CM of normal organoids or MTOs with or without Gal (10 μM) for 72 h (n = 3). Schematic representation (P) and qPCR (Q).
(R) *Prkcz* mRNA levels of CFs stimulated by TGFβ (10 ng/ml) with or without Trichostatin A (TSA) treatment (100 nM) for 48 h (n = 3).
(S) Schematic representation of the epigenetic status of the *PRKCZ* locus in human normal colon crypts and metastases-derived primary CRC cell lines (GSE36204), and in CRC cell lines (GSE73319). H3K27Ac occupancy of *PRKCZ* promoter in human normal colon crypts and metastases-derived primary CRC cell lines (GSE36204), and in CRC cell lines (GSE73319) analyzed by ChIP-seq. Predicted SMAD3/4 and E2F4 binding sites in *PRKCZ* promoter by JASPAR, including relative score and sequence. SMAD3/4 and E2F4 binding motifs from JASPAR.
Results are shown as mean ± s.e.m. *p<0.05, **p<0.01, ***p<0.001, ****p<0.0001. See also Figure S1 and Table S1.

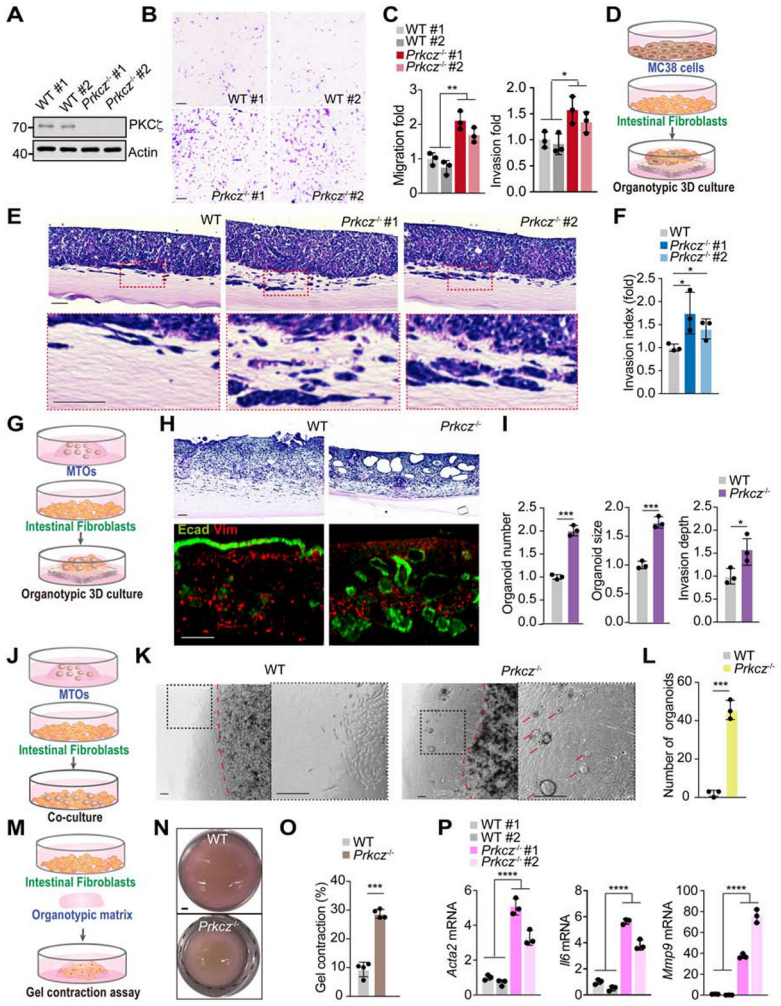

Figure 2. *Prkcz*$^{-/-}$ colonic fibroblasts have CAF characteristics

(A-C) *Prkcz*$^{-/-}$ CFs show more migration and invasion activity. Immunoblot of the indicated proteins in WT or *Prkcz*$^{-/-}$ CFs (A), crystal violet staining of invading MC-38 cells in response to CM of WT or *Prkcz*$^{-/-}$ CFs (B) and quantification (n = 3) (C). Scale bars, 100 μm.

(D-F) 3D Organotypic cultures of MC-38 cells with WT or *Prkcz*$^{-/-}$ CFs (n = 3). Schematic representation (D), H&E staining (E); and quantification of cell invasion (F). Scale bars, 100 μm.

(G-I) 3D Organotypic cultures of MTOs with WT or *Prkcz*$^{-/-}$ CFs (n = 3). Schematic representation (G), H&E staining (top), E-cadherin (green, bottom) and Vimentin (red, bottom) staining (H) and quantification (l) of cell invasion. Scale bars, 100 μm.

(J-L) Direct co-culture assays of MTOs and WT or *Prkcz*$^{-/-}$ CFs (n = 3). Schematic representation (J), microscopic images (K) and quantification of migrating MTOs (L). Scale bars, 50 μm.

(M-O) ECM remodeling assay with WT or *Prkcz*$^{-/-}$ CFs (n = 3). Schematic representation (M), microscopic images (N) and quantification (O). Scale bar, 1 mm.

(P) Relative mRNA expression of the indicated genes in WT or *Prkcz*$^{-/-}$ CFs (n = 3).

Results are shown as mean ± s.e.m. *p<0.05, **p<0.01, ***p<0.001, ****p<0.0001. See also Figure S2.

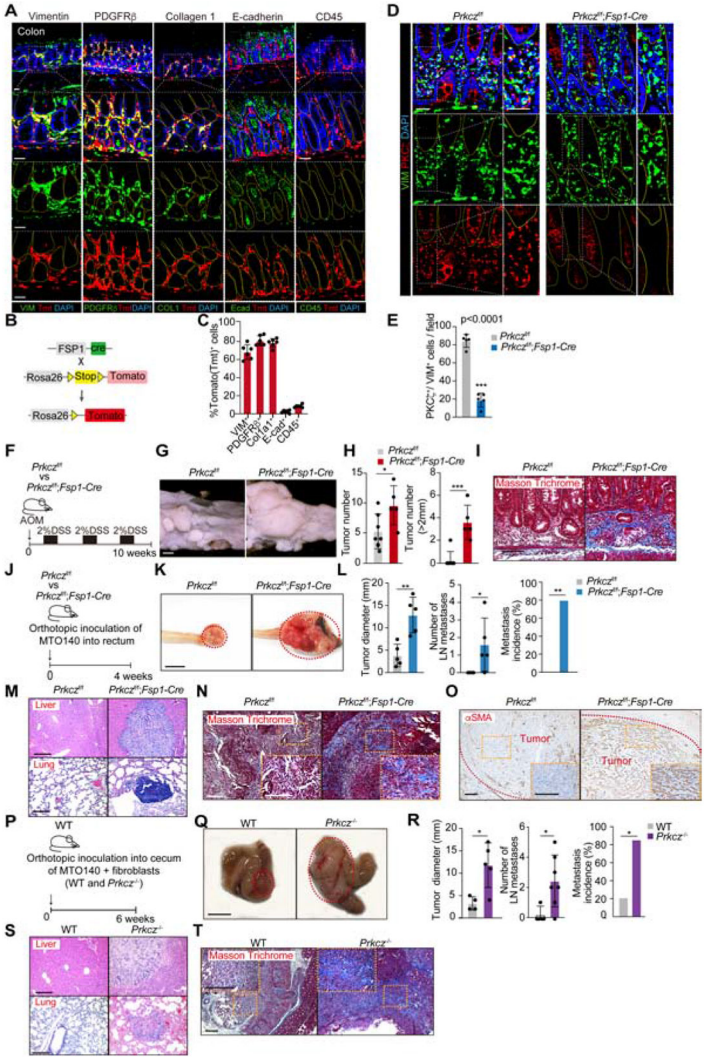

Figure 3. Deletion of PKCζ in colonic fibroblasts promotes tumorigenesis *in vivo*

(A-C) Staining of colon sections from *Fsp1-CreR26R*^{TdT} mice with Vimentin, PDGFRβ, Collagen I, E-cadherin and CD45 (green) and RFP (red) (A), schematic representation of the *Fsp1* and *R26R*^{TdT} locus (B) and quantification (C) (n = 6). Scale bars, 50 μm.

(D and E) PKCζ staining (red) with Vimentin (green) (D) and quantification (E) of colon sections from *Prkcz*$^{f/f}$ and *Prkcz*$^{f/f}$;*Fsp1-Cre* mice (n = 5). Scale bars, 50 μm.

(F-I) *Prkcz*$^{f/f}$, n = 7, and *Prkcz*$^{f/f}$;*Fsp1-Cre,* n = 5, mice (male, 8-10 weeks-old) treated with the azoxymethane (AOM)/DSS protocol. Experimental design (F), macroscopic images (G), quantification of the tumor number (H) and Masson Trichrome staining of colon tumors (I). Scale bars, 1 mm (G), 50 μm (I).

(J-O) Orthotopic inoculation of MTOs in *Prkcz*$^{f/f}$ and *Prkcz*$^{f/f}$;*Fsp1-Cre,* n = 5 mice (male, 6-8 weeks-old) per condition. Experimental design (J), gross images (K), quantification of tumor diameter, number of lymph node metastases and metastasis incidence (L), H&E staining liver and lung metastasis (M), Masson Trichrome staining of tumors (N) and ζSMA staining of the tumors (O). Scale bars, 5 mm (K), 50 μm (M, N and O).

(P-T) Co-implantation into cecum of WT mice (female, 12-18 weeks-old) of MTOs mixed with WT or *Prkcz*$^{-/-}$ CFs (WT, n = 5; *Prkcz*$^{-/-}$, n = 7). Experimental design (P), gross images (Q), quantification of tumor diameter, number of lymph node metastases and metastasis incidence (R), H&E staining of liver and lung metastasis (S) and Masson Trichrome staining of tumors (T). Scale bars, 5 mm (Q) and 50 μm (S and T).
Results are shown as mean ± s.e.m. *p<0.05, **p<0.01, ***p<0.001. See also Figure S3.

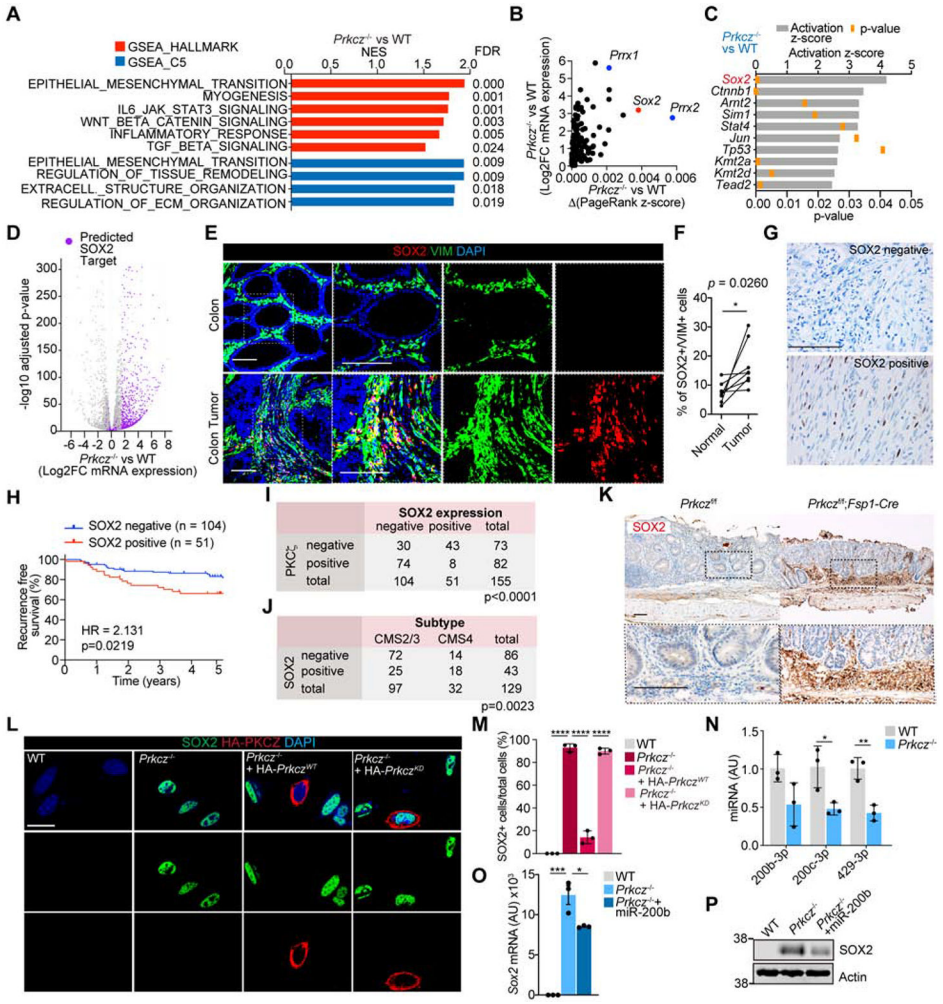

Figure 4. SOX2 is a key transcription factor for fibroblasts activation by PKCζ loss

(A) Top CAF and ECM remodeling pathways from GSEA of *Prkcz*$^{-/-}$ versus WT colonic fibroblasts (CFs), n = 3, using compilations H and C5 (MSigDB). ECM, Extracellular matrix.

(B) Scatterplot of mRNA expression and PageRank z-score for transcription factor genes upregulated in *Prkcz*$^{-/-}$ CFs.

(C) Upstream regulator analysis of the top ranked genes from ATAC-Seq data in *Prkcz*$^{-/-}$ versus WT CFs.

(D) Volcano plot of RNA-Seq of *Prkcz*$^{-/-}$ versus WT CFs. The purple dots represent predicted SOX2 target genes.

(E and F) SOX2 staining (red) with Vimentin (green) (E) and quantification (F) in human CRC samples and normal counterparts (n = 8, paired).

(G) SOX2 staining in human CRC samples.

(H) Kaplan-Meier curve for 5-year recurrence-free survival of CRC patients according to SOX2 expression in stroma (n = 155).

(I) Correlation between PKCζ and SOX2 expressions in CRC stroma (n = 155).

(J) Correlation between SOX2 expression in CRC stroma and CMS subtypes (n = 129).

(K) SOX2 staining of tumors induced by AOM-DSS treatment in *Prkcz*$^{f/f}$ and *Prkcz*$^{f/f}$;*Fsp1-Cre* mice. Scale bar, 50 μm.

(L and M) SOX2 staining (green) with HA (red) (L) and quantification (M) in *Prkcz*$^{-/-}$ versus WT CFs.

(N) qPCR of miR-200s in *Prkcz*$^{-/-}$ versus WT CFs, (n = 3).

(O and P) qPCR for *Sox2* mRNA (O) and immunoblot for SOX2 (P) in *Prkcz*$^{-/-}$ CFs rescued with miR-200b, (n = 3).

Results are shown as mean ± s.e.m. *p<0.05, **p<0.01, ***p<0.001, ****p<0.0001. See also Figure S4 and Table S1.

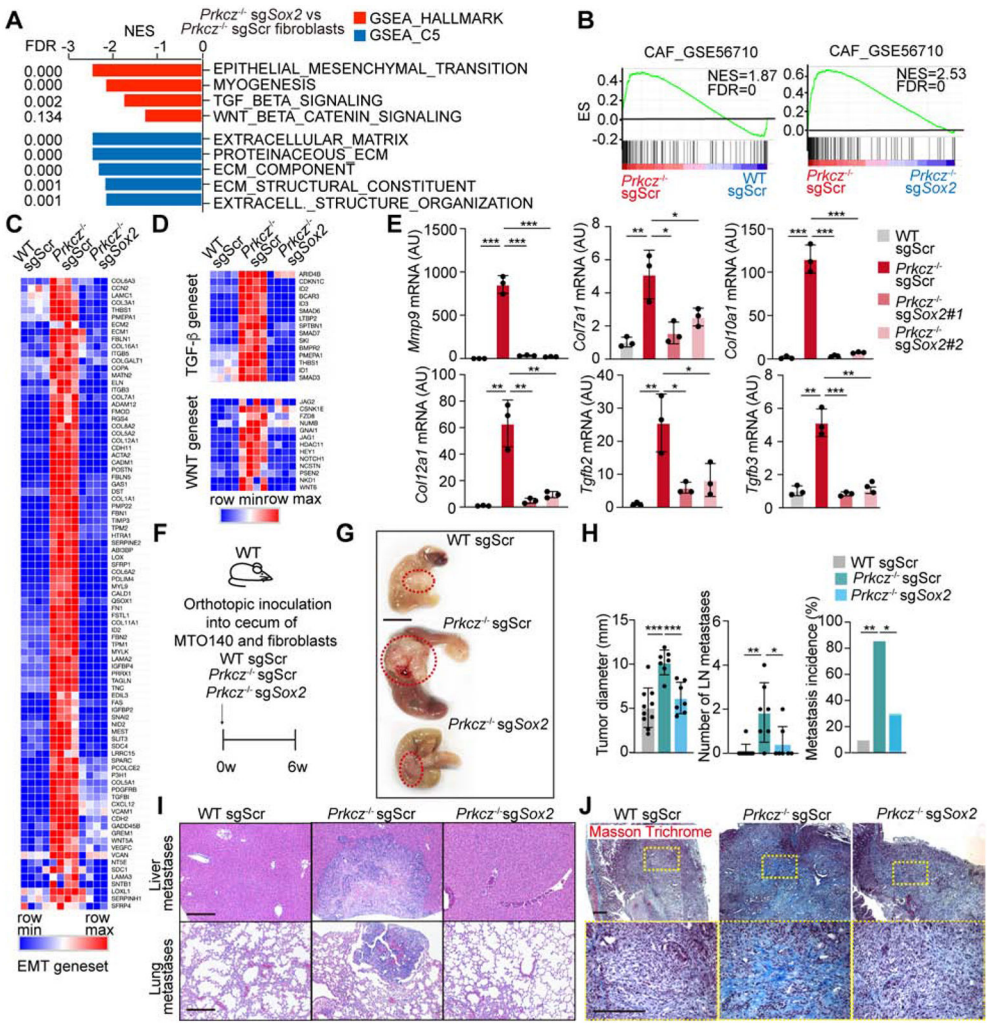

Figure 5. *Sox2* deletion in *Prkcz*$^{-/-}$ colonic fibroblasts rescues the CAF phenotype

(A) Top CAF and ECM remodeling pathways from GSEA of downregulated genes in *Prkcz*$^{-/-}$ sg*Sox2* versus *Prkcz*$^{-/-}$sgScr CFs (n = 4) using H and C5 compilations (MSigDB). ECM, Extracellular matrix.

(B) GSEA plots of enrichment in CAF signature in GSE56710 for WT sgScr versus *Prkcz*$^{-/-}$sgScr CFs (left) and *Prkcz*$^{-/-}$sg*Sox2* versus *Prkcz*$^{-/-}$sgScr CFs (right) (n = 4).

(C and D) Heatmap of reverted genes by *Sox2* deletion associated with "EMT geneset" (C) and "TGFβ and WNT geneset" (D) in *Prkcz*$^{-/-}$ CFs.

(E) mRNA levels of the indicated genes in WT sgScr, *Prkcz*$^{-/-}$ sgScr and *Prkcz*$^{-/-}$sg*Sox2* CFs (n = 3).

(F-J) Orthotopic inoculation into WT mice (female, 7-11 weeks-old) of MTOs mixed with WT sgScr, *Prkcz*$^{-/-}$sgScr or *Prkcz*$^{-/-}$sg*Sox2* CFs (WT sgScr, n = 10; *Prkcz*$^{-/-}$sgScr, n = 7; *Prkcz*$^{-/-}$ sg*Sox2*, n = 7). Experimental design (F), gross images (G), quantification of tumor diameter, number of lymph node and metastasis incidence (H), H&E staining of liver and lung metastasis (I) and Masson Trichrome staining of tumors (J). Scale bars, 5 mm (G), 50 μm (J).

Results are shown as mean ± s.e.m. *p<0.05, **p<0.01, ***p<0.001. See also Figure S5.

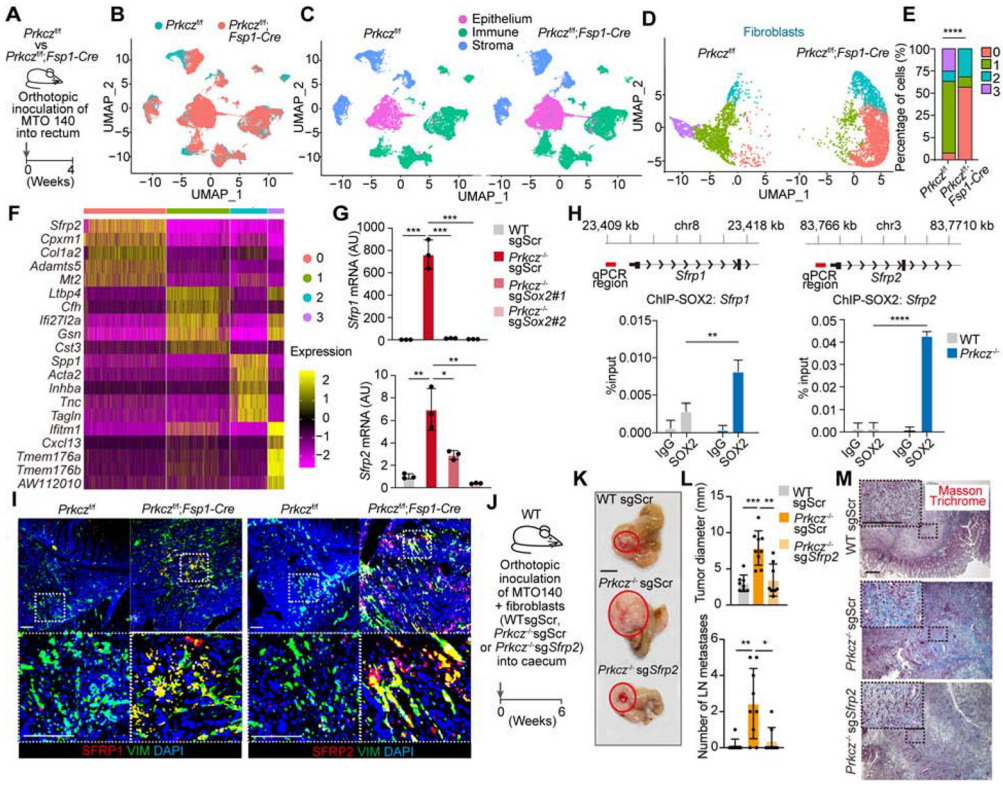

Figure 6. scRNA-Seq identifies a switch in CAF subtypes and *Sfrp1/2* as direct target of SOX2 in *Prkcz*$^{-/-}$ fibroblasts

(A) Experimental design of orthotopic inoculation of MTOs in *Prkcz*$^{f/f}$ and *Prkcz*$^{f/f}$;*Fsp1-Cre* mice (male, 10 weeks-old) for scRNA-Seq.

(B and C) Uniform Manifold Approximation and Projection (UMAP) plot with clustering results colored by sample (B) and by the major cellular compartments (C).

(D) UMAP plot with reclustering of fibroblasts, split by sample.

(E) Stacked bar plots showing the percentage of fibroblasts in each cluster.

(F) Heatmap of the top-5 genes for each cluster.

(G) Relative mRNA expression in CFs of indicated genotype (n = 3).

(H) Primer design and ChIP-qPCR analysis of *Sfrp1* and *Sfrp2* promoter occupancy of SOX2 (n = 3).

(I) SFRP1 (left) and SFRP2 (right) staining (red) with Vimentin (green) in sections from orthotopic tumors in *Prkcz*$^{f/f}$ and *Prkcz*$^{f/f}$;*Fsp1-Cre* mice.

(J-M) Orthotopic inoculation into WT mice (female, 10-13 weeks-old) of MTOs mixed with WTsgScr, *Prkcz*$^{-/-}$sgScr or *Prkcz*$^{-/-}$sg*Sfrp2* Colonic fibroblasts (WTsgScr, n = 8; Prkcz$^{-/-}$sgScr, n = 9; *Prkcz*$^{-/-}$sg*Sox2,* n = 8). Experimental design (J), gross images (K), quantification of tumor diameter and number of lymph node metastases (L) and Masson Trichrome staining of tumors (M). Scale bars 5 mm (K), 50 μm (M).

Results are shown as mean ± s.e.m. *p<0.05, **p<0.01, ***p<0.001, ****p<0.0001. See also Figure S6 and Table S2.

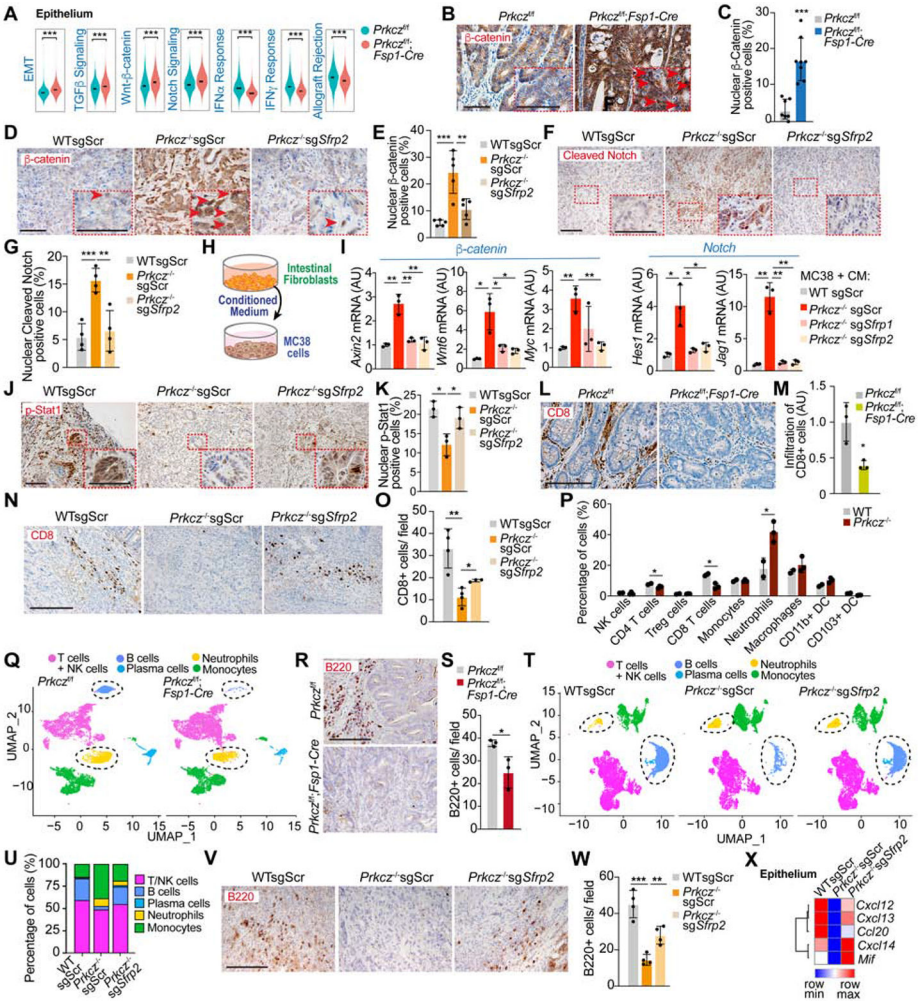

Figure 7. Loss of stromal PKCζ reprograms the tumor epithelium and the immune microenvironment *in vivo*

(A) Violin plots for the indicated gene signatures in epithelial cells from orthotopic tumors in rectum of *Prkcz*$^{f/f}$ and *Prkcz*$^{f/f}$;*Fsp1-Cre* mice.

(B and C) β-catenin staining (B) and quantification (C) of tumors induced by AOM-DSS treatment in *Prkcz*$^{f/f}$ and *Prkcz*$^{f/f}$;*Fsp1-Cre* mice. Scale bar, 25 μm.

(D and E) β-catenin staining (D) and quantification (E) of orthotopic tumors co-implanted in WT mice (female, 10-13 weeks old) with MTOs and WTsgScr or *Prkcz*$^{-/-}$sgScr or *Prkcz*$^{-/-}$sg*Sfrp2* CFs. Scale bar, 25 μm.

(F and G) Cleaved Notch staining (D) and quantification (E) of orthotopic tumors described in (D). Scale bar, 25 μm.

(H and I) qPCR analysis of β-catenin and Notch-related genes of MC38 cells stimulated by conditioned medium (CM) of CFs for 72 h (n = 3). Schematic representation (H) and qPCR (I).

(J and K) Phospho-Stat1 staining (J) and quantification (K) of orthotopic tumors described in (D). Scale bar, 25 μm.

(L and M) CD8 staining (L) and quantification (M) of tumors described in (B). Scale bar, 50 μm.

(N and O) CD8 staining (N) and quantification (O) orthotopic tumors described in (D). Scale bar, 50 μm.

(P) Flow-cytometry analysis of immune cell populations in orthotopic tumors co-implanted with MTOs and WT or *Prkcz*$^{-/-}$ colonic fibroblasts (WT, n = 3; *Prkcz*$^{-/-}$, n = 3).

(Q) UMAP plot of the immune compartment colored by major immune cell types from orthotopic tumors described in (A).

(R and S) B220 staining (R) and quantification (S) of tumors described in (B). Scale bar, 50 μm.

(T) UMAP plot of the immune compartment from orthotopic tumors described in (D).

(U) Stacked bar plots of the percentage of cells in immune compartment.

(V and W) B220 staining (V) and quantification (W) of orthotopic tumors described in (D). Scale bar, 50 μm.

(X) Heatmap of chemokine expression in epithelial cells of orthotopic tumors described in (D). Results are shown as mean ± s.e.m. *p<0.05, ** p<0.01, ***p<0.001.

KEY RESOURCES TABLE

REAGENT or RESOURCE	SOURCE	IDENTIFIER
Antibodies		
Rabbit anti-PKCζ	Abcam	Cat# ab59364; RRID: AB_944858
Rabbit anti-PKCζ	Abcam	Cat# ab225554
Rat anti-Sox2	Invitrogen	Cat# 14-9811-82; RRID: AB_11219471
Rabbit anti-HTR2B	Sigma-Aldrich	Cat# HPA012867; RRID: AB_1856710
Rabbit anti-FRMD6	Abcam	Cat# ab218209
Rabbit anti-CDX2	Novus Biologicals	Cat# NB100-2136; RRID: 10001620
Rabbit anti-ZEB1	Sigma-Aldrich	Cat# HPA027524; RRID: 1844977
Mouse anti-Cytokeratin Pan Type I/II	Invitrogen	Cat# MA5-13156; RRID: 10983023
Rat anti-CD45	BD Biosciences	Cat# 550539; RRID: AB_2174426
Mouse anti-CD8	BD Biosciences	Cat# 550281; RRID: AB_2275792
Rat Anti-CD45R (B220)	Thermo Fisher Scientific	Cat# 17-0452-82; RRID: AB_469396
Rabbit anti-RFP	Rockland	Cat# 600-401-379; RRID: AB_2209751
Mouse anti-αSMA	DAKO	Cat# M0851; RRID: AB_2223500
Rabbit anti-Ki67	Thermo Fisher Scientific	Cat# RM-9106-R7; RRID: AB_149920
Rabbit anti-Chromogranin A	Abcam	Cat# ab45179; RRID: AB_726879
Rabbit anti-SOX9	Sigma-Aldrich	Cat# AB5535; RRID: AB_2239761
Rat anti-CD44	BIO RAD	Cat# MCA4703; RRID: AB_2076194
Mouse anti-E-cadherin	BD Biosciences	Cat# 610181; RRID: 397580
Goat anti-Vimentin	Santa Cruz Biotechnology	Cat# sc-7557; RRID: 793998
Rabbit anti-PDGFR beta	Abcam	Cat# ab69506; RRID: AB_1269704
Mouse anti-Collagen I	Abcam	Cat# ab88147; RRID: AB_2081873
Mouse anti-β-catenin	BD Biosciences	Cat# 610153; RRID: AB_397554
Rabbit anti-pStat1	Cell signaling technology	Cat# 8826; RRID: AB_2773718
Rabbit anti-Cleaved Notch1	Cell signaling technology	Cat# 4147; RRID: AB_2153348
Mouse anti-HA-Tag	Cell signaling technology	Cat# 3724; RRID: AB_1549585
Rabbit anti-Thiophosphate ester antibody	Abcam	Cat# ab92570; RRID: AB_10562142
Mouse anti-Sox2	Santa Cruz Biotechnology	Cat# sc-365823; RRID: 10842165
Rabbit anti-Sfrp1	Abcam	Cat# ab4193; RRID: 304357
Rabbit anti-Sfrp2	Abcam	Cat# ab137560
Rabbit anti-Sox2	Cell signaling technology	Cat# 23064; RRID: AB_2714146
Rabbit anti-Histone H3K27me3	Active motif	Cat# 39055; RRID: AB_2561020
Rabbit anti-Histone H3K4me3	Active motif	Cat# 39159; RRID: AB_2615077
Rat anti-CD16/CD32	BD Pharmingen	Cat# 553142, RRID: AB_394657
Rat anti-CD45	BD Horizon	Cat# 563891, RRID: AB_2734134
Hamster anti-TCRβ chain	BD Pharmingen	Cat# 553174, RRID: AB_398534
Armenian hamster anti-TCRβ chain	eBioscience	Cat# 45-5961, RRID: AB_925764

REAGENT or RESOURCE	SOURCE	IDENTIFIER
Mouse anti-NK1.1	BD Pharmingen	Cat# 553165, RRID: AB_394677
Rat anti-CD4	BD Horizon	Cat# 560468, RRID: AB_1645271
Rat anti-CD8	BD Pharmingen	Cat# 557654, RRID: AB_396769
Rat anti-CD25	eBioscience	Cat# 17-0251, RRID:AB_469365
Armenian hamster anti-CD11c	BD Pharmingen	Cat# 558079, RRID:AB_647251
Rat anti-CD11b	eBioscience	Cat# 47-0112, RRID:AB_1603193
Rat anti-F4/80	eBioscience	Cat# 12-4801, RRID:AB_465923
Rat anti-Ly6C	BD Horizon	Cat# 560594, RRID:AB_1727559
Rat anti-Ly6G	BD Pharmingen	Cat# 561236, RRID:AB_10611860
Armenian hamster anti-CD103	eBioscience	Cat# 48-1031, RRID:AB_2574033
Rat anti-CD19	BD Pharmingen	Cat# 550992, RRID:AB_398483
Mouse anti-β-actin	Sigma-Aldrich	Cat# A1978, RRID:AB_476692
Goat anti-Mouse IgG, secondary, HRP	Thermo Fisher Scientific	Cat# 31436, RRID: AB_228313
Goat anti-Mouse IgG1, secondary, HRP	Thermo Fisher Scientific	Cat# PA1-74421, RRID: AB_10988195
Goat anti-Rabbit IgG, secondary, HRP	Thermo Fisher Scientific	Cat# 31461, RRID: AB_228347
Goat anti-Rabbit IgG, secondary, IRDye 800	LI-COR Biosciences	Cat# 926-32211, RRID: AB_621843
Goat anti-Rat IgG, secondary, IRDye 800	LI-COR Biosciences	Cat# 926-32219, RRID: AB_1850025
Goat anti-Mouse IgG, secondary, IRDye 800	LI-COR Biosciences	Cat# 926-32210, RRID: AB_621842
Goat anti-Mouse IgG1, secondary, Alexa Fluor 488	Thermo Fisher Scientific	Cat# A21121, RRID: AB_2535764
Donkey anti-Rat IgG, secondary, Alexa Fluor 488	Thermo Fisher Scientific	Cat# A21208, RRID: AB_2535794
Donkey anti-Rabbit IgG, secondary, Alexa Fluor 568	Thermo Fisher Scientific	Cat# A10042, RRID: AB_2534017
Donkey anti-Goat IgG, secondary, Alexa Fluor 488	Thermo Fisher Scientific	Cat# A11055, RRID: AB_2534102
Donkey anti-Goat IgG, secondary, Alexa Fluor 568	Thermo Fisher Scientific	Cat# A11057, RRID: AB_142581
Goat anti-Mouse IgG, secondary, Alexa Fluor 568	Thermo Fisher Scientific	Cat# A11004, RRID: AB_2434072
Biological Samples		
Human colon samples (Normal colon tissues, sessile serrated adenomas/polyps, tubular adenomas)	Scripps Green Hospital, La Jolla, USA	N/A
Human Colorectal cancers (CRCs)	Osaka City University Hospital, Osaka, JAPAN	N/A
Chemicals, Peptides, and Recombinant Proteins		
PBS (no calcium, no magnesium)	Thermo Fisher Scientific	Cat# 10010-023
HBSS (no calcium, no magnesium)	Thermo Fisher Scientific	Cat# 14175095
Tryple Express	Life Technologies	Cat# 12605-010
DMEM	Corning	Cat# 10-017CV
Advanced DMEM/F12	Thermo Fisher Scientific	Cat# 12634010
GlutaMAX Supplement	Thermo Fisher Scientific	Cat# 35050061
HEPES	Thermo Fisher Scientific	Cat# 15630080
B27 Supplement minus vitamin A	Thermo Fisher Scientific	Cat# 12587001
Murine EGF	Thermo Fisher Scientific	Cat# PMG8045
Recombinant Mouse TGF-beta 1 Protein	R&D	Cat# 7666-MB

REAGENT or RESOURCE	SOURCE	IDENTIFIER
Galunisertib (LY2157299)	Dr. Eduard Batlle (Institute for Research in Biomedicine, Barcelona, Spain)	N/A
Trichostatin A	Sigma-Aldrich	Cat# T8552
Recombinant Human SOX2 protein	Peprotech	Cat# 110-03-25UG
Recombinant PKCi kinase	Panvera	Cat# PV3186
Recombinant PKCz kinase	Invitrogen	Cat# P2268
Liberase™ TM Research Grade	Sigma-Aldrich	Cat# 5401119001
Collagenase type XI	Sigma-Aldrich	Cat# C7657
Cultrex® Basement Membrane Matrix, Type 2	Trevigen	Cat# 3532-001-02
TRIzol	Thermo Fisher Scientific	Cat# 15596018
Trypsin-EDTA (0.25%), phenol red	GIBCO	Cat# 25200056
Lipofectamine RNAiMAX	Thermo Fisher Scientific	Cat# 13778150
X-tremeGENE transfection reagent	Roche	Cat#6366236001
TrueCut Cas9 Protein v2	Thermo Fisher Scientific	Cat# A36498
Matrigel basement membrane matrix	Corning	354234
Collagen type I	Corning	354236
ECL Western Blotting Substrate	Thermo Scientific	Cat# 32106
DAPI	Life Technologies	Cat# D1306
Azoxymethane	Sigma-Aldrich	Cat# A5486
Dextran Sulfate Sodium Salt (DSS) - Colitis Grade (36,000 - 50,000 MW)	MP biomedicals	CAS Number: 9011-18-1
Critical Commercial Assays		
VECTASTAIN® Elite® ABC-HRP Kit	Vector	Cat# PK-6100
Matrigel invasion assay	Corning	354480
Migration assay	Corning	354578
In Situ Cell Death Detection Kit, TMR red	Sigma-Aldrich	Cat# 12156792910
Trichrome Stain (Masson) Kit	Sigma-Aldrich	Cat# HT15
Neon™ 10µl Electroporation Kit	Thermo Fisher Scientific	Cat# MPK1096
Neon™ Transfection System	Thermo Fisher Scientific	Cat# MPK5000
ChIP-IT® Express Enzymatic Shearing Kit	Active motif	Cat# 53035
Deposited Data		
RNA-Seq (WT and *Prkcz*$^{-/-}$)	This study; GEO	GSE154843
ATAC-Seq (WT and *Prkcz*$^{-/-}$)	This study; GEO	GSE154857
RNA-Seq (WT sgScr, *Prkcz*$^{-/-}$ sgScr and *Prkcz*$^{-/-}$ sg*Sox2*)	This study; GEO	GSE154852
scRNA-Seq (*Prkcz*$^{f/f}$ and *Prkcz*$^{f/f}$*Fsp1-Cre*)	This study; GEO	GSE154863
scRNA-Seq(WT sgScr, *Prkcz*$^{-/-}$ sgScr and *Prkcz*$^{-/-}$ sg*Sfrp2*)	This study; GEO	GSE157697
Raw Data	This study; Mendeley Data	https://doi.org/10.17632/5syy6gf4bw.1
Experimental Models: Cell Lines		
Human HEK293T	ATCC	Cat# CRL-3216, RRID:CVCL_0063

REAGENT or RESOURCE	SOURCE	IDENTIFIER
Human Phoenix-GP	ATCC	Cat# CRL-3215, RRID:CVCL_H718
Mouse MC38	Kerafast	Cat# ENH204, RRID:CVCL_B288
Mouse tumor organoid (MTO)	(Tauriello et al., 2018)	N/A
Experimental Models: Organisms/Strains		
Mouse: *Prkcz*$^{-/-}$	(Leitges et al., 2001)	N/A
Mouse: *Prkcz*$^{f/f}$	(Llado et al., 2015)	N/A
Mouse: *Prkcl/i*$^{f/f}$	(Leitges et al., 2001)	N/A
Mouse: *R26R*^{TdT}	Gift from Alessandra Sacco, Ph.D.	N/A
Mouse: BALB/c-Tg(S100a4-cre)1Egn/YunkJ (*Fsp1-Cre*)	The Jackson Laboratories	Stock No: 012641
Mouse: NOD.Cg-*Prkdc*^{scid} *Il2rg*^{tm1Wjl}/SzJ (NSG)	The Animal Facility Core at SBP Medical Discovery Institute	N/A
Oligonucleotides		
Real-time PCR primers	This paper	Table S3
gRNA targeting mouse *Sox2* gene: (5′ CUCCAUCAUGUUAUACAUGC)	https://www.synthego.com/	N/A
gRNA targeting mouse *Sfrp1* gene: (5′ UCGCCGAGCAACAUGGGCGU)	https://www.synthego.com/	N/A
gRNA targeting mouse *Sfrp2* gene: (5′ UUCACACACCUUGGGAGCUG)	https://www.synthego.com/	N/A
siRNA targeting mouse *Sfrp1* gene	Santa Cruz	Cat# sc-39999
siRNA targeting mouse *Sfrp2* gene	Santa Cruz	Cat# sc-40001
mirVana miRNA mimic, negative control	Invitrogen	Cat# 4464058
mirVana miRNA mimic, hsa-miR200b-3p	Invitrogen	Cat# 4464066
Recombinant DNA		
pMXs-Sox2-IP	Addgene	Cat# 15919; RRID:Addgene_15919
pLenti6.3/V5-DEST-SFRP1	DNASU	Cat# HsCD00936572
pLenti6.3/V5-DEST-SFRP2	DNASU	Cat# HsCD00938859
Software and Algorithms		
ImageJ	NIH	https://imagej.nih.gov/ij/
Graphpad Prism 8	Graphpad	https://www.graphpad.com/scientific-software/prism/
ImageProPlus 6	MediaCybernetics	N/A
GenePattern	Broad Institute	https://genepattern.broadinstitute.org/gp/pages/index.jsf
GSEA (v7.0)	Broad Institute	http://www.broadinstitute.org/gsea/index.jsp
IPA	QIAGEN	N/A
BaseSpace	Illumina	https://basespace.illumina.com
Morpheus	Broad Institute	https://software.broadinstitute.org/morpheus/
Samtools 1.9	Li et al., 2009	http://samtools.sourceforge.net/
MACS2 (2.1.0)	Feng et al., 2012	https://github.com/taoliu/MACS

REAGENT or RESOURCE	SOURCE	IDENTIFIER
Picard (v2.18.14)	Broad Institute	https://broadinstitute.github.io/picard/
DEseq2(1.18.1)	Love et al, 2014	https://bioconductor.org/packages/release/bioc/html/DESeq2.html
deeptools (3.0.2)	Ramirez et al., 2016	https://github.com/deeptools/deepTools
IGV (v2.4.13)	Broad Institute	https://software.broadinstitute.org/igv/
R (3.5.1)	R Core Team	https://www.r-project.org/
RStudio (1.1.456)	R Core Team	https://www.r-project.org/
ChIPSeeker (3.6)	Yu et al., 2015	https://github.com/GuangchuangYu/ChIPseeker
Cell Ranger (v3.0)	10X genomics	http://software.10xgenomics.com/single-cell/overview/welcome
Seurat 3.0	Stuart et al., 2019	https://github.com/Satijalab/seurat
Lexogen QuantSeq DE 1.3.0	BlueBee Cloud	https://www.bluebee.com
FlowJo 10.0	Flowjo	https://www.flowjo.com
Other		
Zeiss LSM 710 NLO Confocal Microscope	Carl Zeiss Microscopy	N/A
EVOS XL Core Cell Imaging System	Thermo Fisher Scientific	N/A
NanoDrop 1000 spectrophotometer	Thermo Fisher Scientific	N/A